PEROVSKITE ELECTROCATALYSTS FOR

THE OXYGEN EVOLUTION REACTION

by

Ning Wang

A thesis submitted to Johns Hopkins University in conformity with the requirements for the degree of Master of Science in Engineering

Baltimore, Maryland

Aug, 2014

ABSTRACT

To commercialize clean-energy technologies such as water electrolyzers and fuel cells, highly efficient electrocatalysts are needed to improve the kinetics of the oxygen evolution reaction (OER). Perovskites have recently received substantial interest as they could be more cost-effective than, while possess comparable catalytic activities with, the state-of-the-art IrO_2 and RuO_2 electrocatalysts for the OER. While the previous studies are mostly reported on thin-film or micrometer-scale catalysts, this work aims to develop advanced perovskite nanocatalysts for the OER. $LaMO_3$ (M=Ni, Co, Fe, Mn) perovskite nanocatalysts (5─300 nm) are synthesized by sol-gel methods, with the morphological and crystalline sizes controlled by tuning the protocols of calcination and/or using silica templates. These materials are characterized by transmission electron microscopy (TEM), scanning electron microscope (SEM), and X-ray diffraction (XRD). Electrocatalytic performance towards the OER is studied in alkaline solution by using a rotating disk electrode (RDE) and a three-electrode electrochemical cell. It is found that the catalytic performance of different perovskites of similar sizes follows the trend: La_2NiO_4> $LaNiO_3$>$LaCoO_3$>$LaMnO_{3+\delta}$>$LaMnO_3$>$LaFeO_3$, consistent with previous results obtained on microcrystalline catalysts. The two Ni perovskite catalysts are found to show interesting redox peaks during the OER which could be assigned to Ni^{2+}/Ni^{3+} conversion. In addition, size-dependent electrocatalytic performance of the perovskite catalysts is revealed by studying $LaCoO_3$ catalysts of different sizes. In general, smaller particles give higher mass activity, except the nanoporous $LaCoO_3$ made with silica template. The

later, however, shows smaller Tafel slope than the other catalysts with larger crystalline sizes. This indicates that the intrinsic (surface-specific) catalytic activity and kinetics of the OER improves with decreasing particle size, while the relatively low mass activity of nanoporous $LaCoO_3$ could be due to mass transportation limits within the nanoscale pores. These findings represent important steps toward development of high-surface-area, precious metal-free catalysts for electrical-chemical energy conversion and fundamental understanding of the structure-property relationships of metal oxide nanomaterials in electrochemical reaction environments.

Reader (Thesis advisor): Professor Chao Wang

Reader: Professor Jonah Erlebacher

ACKNOWLEDGEMENT

First of all, I would like to thank my advisor, Prof. Chao Wang, for guidance on my research in these two years. I also would like to thank David Raciti, Yifan Liu and Matthew Gonzalez for help on nanoparticle synthesis and/or electrochemical studies. Moreover, I would like to thank Prof. Jonah Erlebacher for reviewing my thesis and providing comments for improvement. Finally, I would like to thank my family for supporting my graduate studies.

Table of Contents

List of Tables

List of Figures

Chapter 1 Introduction to catalyst in energy research

1.1 Energy and energy storage

The thriving population and booming economy, against depletion of fossil fuels, bring about urgent need for clean and renewable energy technologies. In the modern society, as the paramount energy source, fossil fuels support the industries and economic growth. According to 2011 statistics from International Energy Agency (IEA), fossil fuels such as crude oil, coal and natural gas accounted for about 80% in primary energy usage in the world. About 10,000 million tons of petroleum were consumed in year of 2000 which is presumably to be doubled by the year of 2030 as predicted.[1] However, unlike the rapid speed of extraction, the formation and accumulation of fossil fuels usually take millions of years before their usage becomes practicable. The increasing price of fossil fuels especially the oil price indicates that fossil fuels are reaching their peak of supplies. On the other hand, considerable amount of CO_2 was emitted during fossil fuel consumption. As a greenhouse gas, CO_2 is very difficult to be deactivated from atmosphere, and thus will elevate global temperature and aggravate the warming problem as shown in

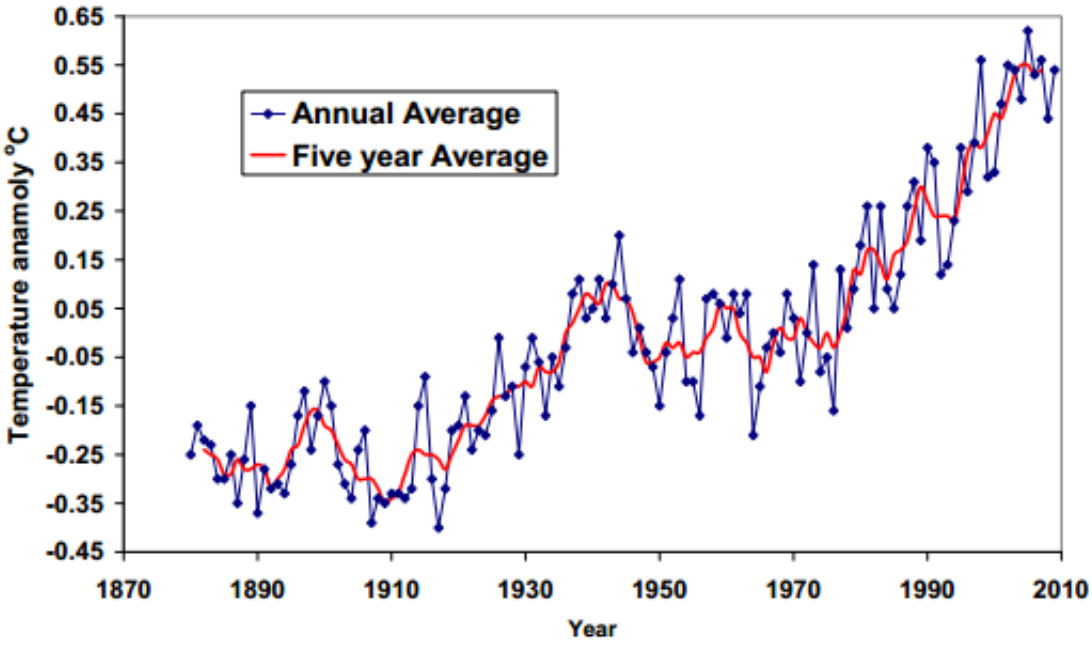

Figure *1*. It turns out that the simultaneous increment in average worldwide temperatures, as known as global warming was related to the growth of CO_2 concentration in atmosphere over years. Researchers estimated that approximately one billion tons of CO_2 would be produced and emitted into atmosphere by the year of 2053 if the situation is left without any human intervention. [2-4]

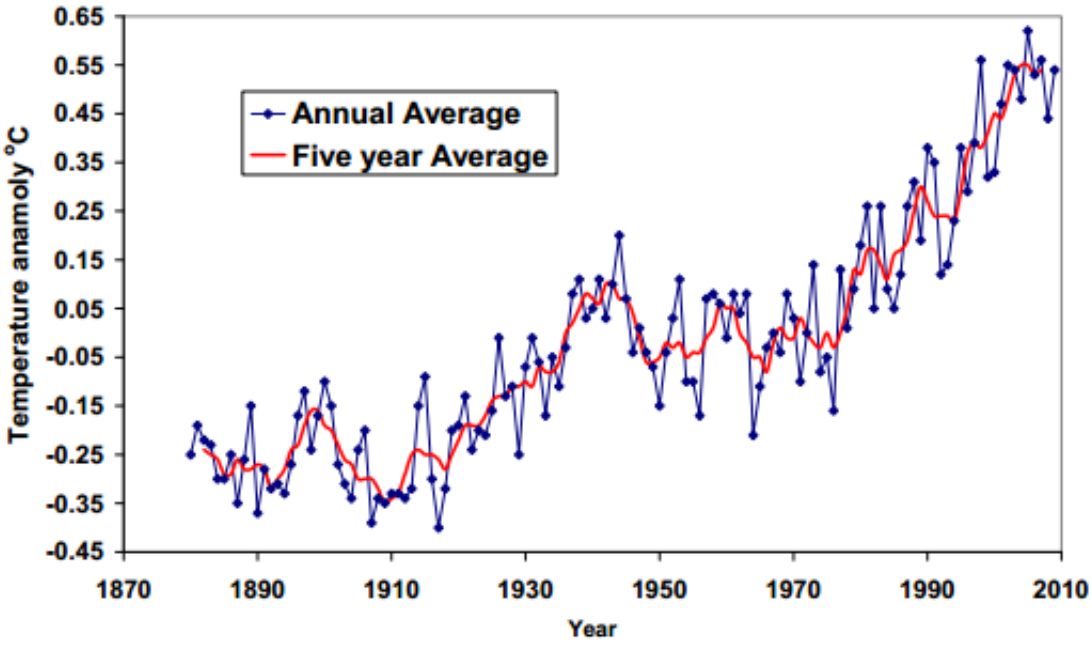

Figure 1 Plot of global instrumental temperature anomaly vs. time.

The most important renewable energy source would be solar, considering sunlight almost irradiates everywhere and has powered lives on earth for millions of years by plants through photosynthesis. Approximately about 128,000 ZJ (10^{21}J) of solar radiation arrives on the Earth every year. [6] The sun radiation could be converted into electrical power directly by utilizing photovoltaics (PV). However, solar energy is intermittent and thus devices that can store solar electricity are needed. While batteries are widely used for energy storage in portable electronics and electrical vehicles, they may not be suitable for large-scale applications, e.g., grid, due to the poor cost effectiveness and technical barriers in scaling up. Alternatively, the electrical power generated from solar cells can be utilized to produce hydrogen through water electrolysis and store the energy in a chemical form. The obtained hydrogen can then be used to power fuel cells and generate electricity for further use. With hydrogen as the carrier of energy, the combination of

solar cells, electrolyzers and fuel cells represent a renewable energy scheme based on electrochemical energy conversion and storage, which could relieve our relying on fossil fuels and mitigate carbon dioxide emission. [7-9]

1.2 Fuel cells and electrolysis

1.2.1 Fuel cells

Fuel cell is an electrochemical device that converts chemical energy from fuel directly into electricity through a chemical reaction. The most common fuel used in fuel cell is hydrogen while hydrocarbons such as methanol can also be used.

The basic design of fuel cells can be dated back to 1801 when Humphry Davy discovered several new metals such as potassium and sodium in the electrolysis research. In this research voltaic pile was used to split up common compounds. This is remarked as the foundations for fuel cells in the scientific research. [10-11] After thirty seven years, another scientist named Christian Friedrich Schönbein designed the fuel cell. [12] In the next year, Welsh chemical-physicist William Robert Grove proved that the electrical current was produced during an electochemical reaction of oxygen with hydrogen in the first crude fuel cell. Since he used a combination of metal and acid, this fuel cell was very similar to today's phosphoric-acid fuel cell. [13-14]. Ludwig Mond and Charles Laner obtained 20 Am^{-2} at 0.73V by using coal to serve as the fuel. Through improvement by British engineer Francis Bacon in 1932, a 5 kW stationary fuel cell as the first alkaline fuel cell was obtained as the first alkaline fuel cell. After that, this stationary fuel cell was modified by W. Thomas Grubb in General Electric Company and then Leonard Niedrach.

Thomas used a sulphonarted polystyrene ion-exchange membrane as electrolyte while he deposited platinum on this membrane serving as catalyst for reaction. This polymer electrolyte membrane fuel cell was known as the “Grubb-Niedrach fuel cell”. [15-16] This Grubb fuel cell was used in McDonnell Aircraft in Project Gemini, a space mission leaded by NASA. Later, in another space mission, an Alkali Fuel Cell providing 1.5 KW energy was used. Besides electricity, this fuel cell can provides drinking water due to the hydrogen reaction. In the following space shuttle, scientists succeeded to invent a 12 KW Alkali Fuel Cell. Since 1970 the electric vehicle has drawn more and more attention. This stimulated the commercialization of Fuel cells [16-18].

Alkaline fuel cells are one the most efficient types of fuel cells. Figure 2 illustrated this device. On the anode, fuel such as hydrogen is oxidized to produce water and electrons. On the cathode, oxygen is reduced to produce hydroxyl ions. The hydroxyl ions transfer from cathode to anode and the electrons flow through external circuit.

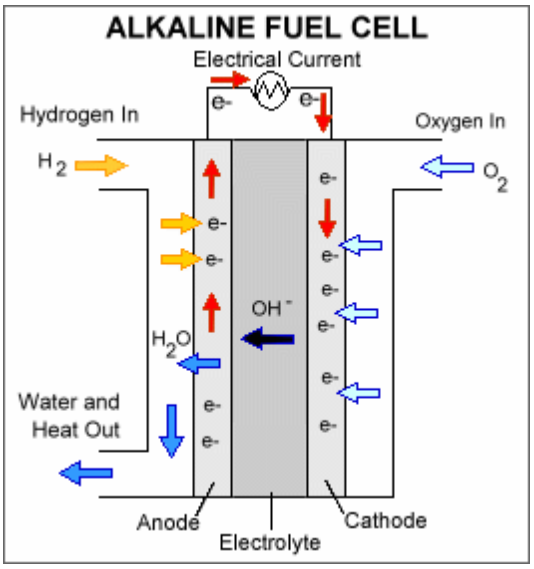

Figure 2 Scheme of alkaline fuel cells

1.2.2 Electrolysis of water

The invention of electrolysis of water can be dated back to the first industrial revolution in the year of 1800. [19] It was discovered by William Nicholson and Anthony Carlisle.

In 1789, J.R. Deiman and A.P. van Troostwijk applied an electrostatic generator to charge water through two gold wires. And evolution of gases happened. [20] After the invention of the voltaic pile in 1800 by Alessandro Volta, William Nicholson and Anthony Carlisle repeated the experiment of electrolysis of water. [21] Also, the gases generated during this process were identified to be hydrogen and oxygen. Faraday's law of electrolysis established the proportional relationship between electrical energy consumption and the amount of gases generated. As a result, researchers began to understand and acknowledge the concepts along with the principles of electrolysis of water. [22] In 1869, Zénobe Gramme invented the Gramme machine. After that, electrolysis of water became an economical method in the field of hydrogen production. In 1888, it became a technique used in the industrial production of hydrogen and oxygen. Following that, there were about 400 electrolyzers operating in the industrial hydrogen production. [23] The electrolyzer is illustrated in Figure 3. [24]

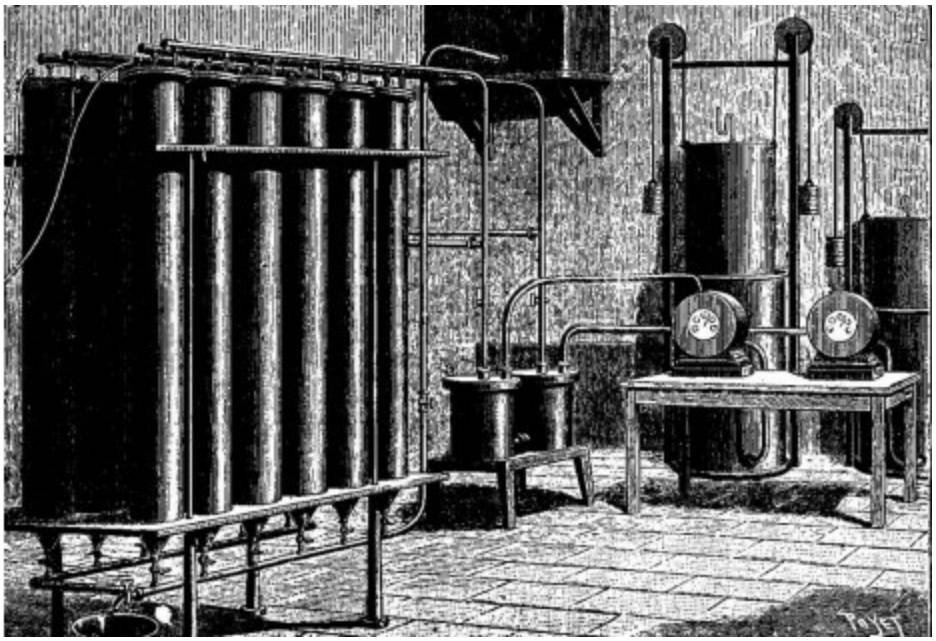

Figure 3 Early plants for the industrial electrolysis of water

The golden age for the development of electrolysis of water occurred in the years between 1920s and 1970s. During that period, numerous traditional devices were invented. In 1939, the first large-scale water electrolysis plant came into operation with a capacity of 10,000 Nm^3 H_2/h. Following that was the manufacture of the first pressurized electrolyzer built by Zdansky/Lonza. In 1966 General Electric created the first solid polymer electrolyte system. A lot of the technological components involved in these designs are still in use nowadays. [25]

Due to the crisis of petroleum in 1970s, electrolysis of water drew attention of scientists again. The first solid oxide water electrolysis unit was invented at that time. And alkaline electrolysis came to industrial field in 1978. With the several technological developments, electrolysis of water serves our society in recent years. These techniques are as follows: proton exchange membranes by DuPont, high temperature solid oxide technology and reconstruction of alkaline water electrolyzers. [26]

1.2.3 Alkaline electrolyzers

Water electrolysis can be performed in acid, alkaline or neutral electrolytes. In practice, an ion-selective membrane is usually implemented to avoid ion polarization in the system. This makes alkaline and acid electrolyzers more feasible than electrolysis in neutral electrolytes as proton- (e.g., Nafion) or anion-exchange (e.g., doped polybenzimidazole) membranes are readily available. [27]

The structure of alkaline electrolyzer is shown in Figure 4. Two water molecular are reduced to hydrogen and two hydroxyl ions. And this process is named as hydrogen evolution reaction. On the anode, hydroxyl ions are oxidized into oxygen. There is a membrane between these two electrodes. It allows hydroxyl ions to pass and transport from cathode to anode.

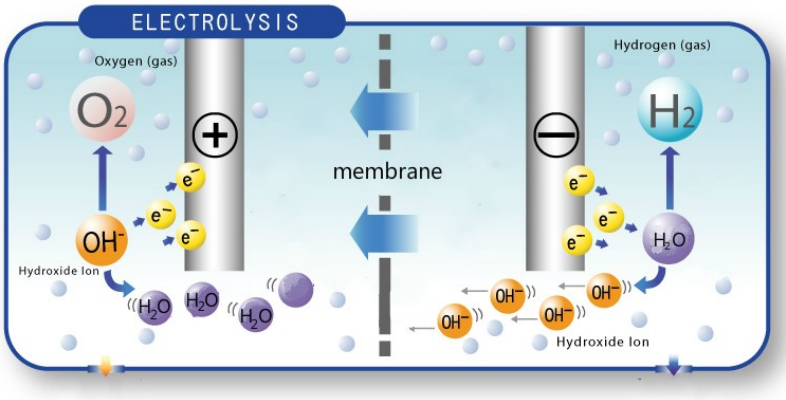

Figure 4 Structure of alkaline electrolyzer [28]

One example of the alkaline electrolyzer was manufactured by GHW Company. The hydrogen produced in this electrolyzer was delivered under high pressure normally as 30 bar. In a pressure vessel, a bipolar cell stack is consisted of electrode-diaphragm units. Also this cell stack is surrounded by the water for electrolysis. As a result, it is designed

to have no pressure difference between the inside part and the outside part of cell stack. Furthermore, the lye is separated from air and the water.

1.2.4 Principles in water electrolysis

Figure 5 elucidats the simplest core unit in water electrolysis. It consists anode, cathode and the external power. The anode and cathode are connected through an electrical cycle with supplement of external power. [29] The hydrogen is generated on the anode which is connected to the positive electrode while oxygen is produced on the cathode which is connected to the negative electrode. In addition, the amount of hydrogen generated on cathode is always the twice of that for oxygen on anode.

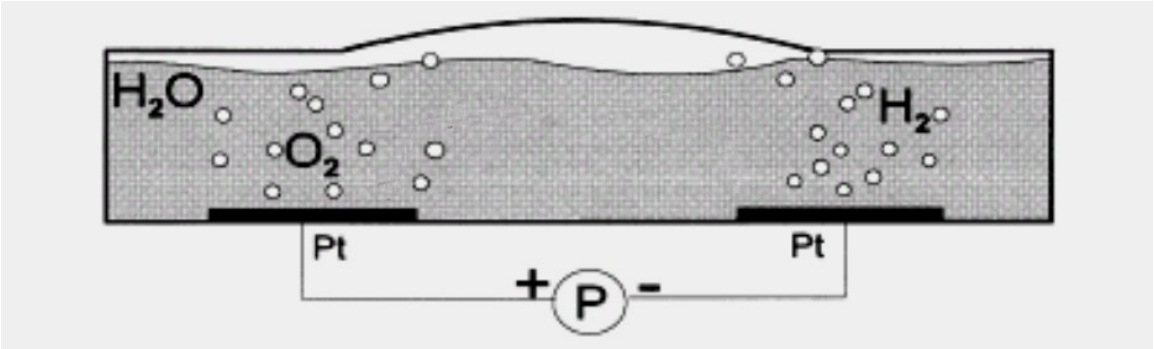

Figure 5 Sketch of the process happened during electrolysis of water [27]

Overall reaction: $2\ H_2O\ (l) \rightarrow 2\ H_2\ (g) + O_2\ (g)$

Since the electrical energy should be taken into consideration here, a new form of work should be inserted into principle of thermodynamics.

$$dU = TdS - pdV + dW_{other}$$

With the Legendre transformation, Gibbs free energy can be calculated:

$$G = U + pV - TS$$

And for the processes at constant temperature and pressure, change of free energy equals the maximum non-expansion work in the system.

$$\Delta G_{reaction} = W_{non-pV,max}$$

The work done on an electrochemical cell can be defined as:

$$-W_{electro} = -nFE$$

In a reversible electrochemical cell, work done on a reversible electrochemical cell is the non-expansion work. Here comes the following equation.

$$E^0_{cell} = {-\Delta G^0}/{nF}$$

And ΔG^0 for this reaction could be calculated through the difference between standard free energy values for products and reactants. The value of ΔG^0 can also be expressed in the formation of enthalpy change and entropy change.

$$\Delta G_{reaction} = \Delta H_r - T\Delta S_r$$

Form standard entropy and enthalpy chart, the entropy change for this reaction is 571.66 KJ/mol and the enthalpy change is 326.686 J/mole. Then the free energy change can be calculated as 474.3075 KJ/mol. And the potential in revisable cell, the revisable potential is 1.23V.

However, this is normally conducted in different kinds of solutions. It goes through different pathways in solution of different pH. In the acid the typical equation is shown below.

Reduction at cathode: $2\ H^+(aq) + 2e^- \rightarrow H_2(g)$ $E^0 = 0.00$ V vs. SHE

Oxidation at anode: $2\ H_2O(l) \rightarrow O_2(g) + 4\ H^+(aq) + 4e^-$ $E^0 = 1.23$ V vs. SHE

While in the alkaline solution where a strong base is added as electrolyte. The hydroxide anions will move to the surface of anode and lose electrons while there is no hydrogen ion involved in this process.

Cathode (reduction): $2\ H_2O(l) + 2e^- \rightarrow H_2(g) + 2\ OH^-(aq)$ $E^0 = -0.83$ V vs. SHE

Anode (oxidation): $4\ OH^-(aq) \rightarrow O_2(g) + 2\ H_2O(l) + 4e^-$ $E^0 = 0.40$ V vs. SHE

The overall reaction is the same and the theoretical cell voltage is the same as 1.23V.

However the electrolysis of water usually requires excess energy to overcome the activation barriers. If the energy is provided just above the potential at equilibrium, the electrolysis is very hard to happen or it will process slowly. As a result the real potential is larger than 1.23V. The difference between the theoretical potential and the operation potential is known as the overpotential. As reported in study from Y. Matsumoto and E. Sato, [30] experimental overpotential of RuO_2 is about 0.6 V and that of IrO_2 is around 0.7. For MnO_2, the overpotential could even reach 0.9 V nearly 75% of the theoretical potential. All the overpotentials above are reported at 10 $mAcm^{-2}$.

1.3 OER and the catalyst

1.3.1 Oxygen evolution reaction

The oxidation reaction happened on the anode is named as oxygen evolution reaction since it generate the oxygen.

$$4\ OH^-\ (aq) \rightarrow O_2\ (g) + 2\ H_2O\ (l) + 4e^-$$

However, the OER has a really sluggish kinetics even though it is facilitated by a high-active and precious catalyst. This limitation keeps itself as an obstacle on the way of commercializing of electrolysis of water and the related devices relied on the hydrogen generated from electrolysis of water.[32] As the state of the art, iridium oxide (IrO2) and RuO_2 are employed as the catalyst for the OER while they are underperformed and expensive. [33] This limitation is associated with the substantial overpotential and the energy loss caused by the overpotential. As a result, new effective catalysts for the OER are need, which should be able to reduce the overpotential of the OER and also stable during the OER. And they should be affordable for industrial compared to the IrO_2 and RuO_2. [34]

1.3.2 Descriptor for the OER catalyst

Jan Rossmeisl's [35] group divided the OER into four paths since this reaction involves four electron. And the asterisk (*) stands for the catalyst during these four paths during the OER. A method based on density functional calculation was applied. [36-38] The four steps and their free energy change sare shown in the following equations. The

free energy for each step is calculated by standard hydrogen electrode which replaces one proton and one electron with half hydrogen molecule probably when potential is about 0V vs SHE.

$$H_2O\ (l) + * \leftrightharpoons HO^* + H^+ + e^-$$

$$\Delta G_1 = \Delta G_{HO^*} - \Delta G_{H2O(l)} - eU + K_b T \ln a_{H+}$$

$$HO^* \leftrightharpoons O^* + H^+ + e^-$$

$$\Delta G_2 = \Delta G_{O^*} - \Delta G_{HO^*} - eU + K_b T \ln a_{H+}$$

$$O^* + H_2O\ (l) \leftrightharpoons HOO^* + H^+ + e^-$$

$$\Delta G_3 = \Delta G_{HOO^*} - \Delta G_{O^*} - eU + K_b T \ln a_{H+}$$

$$HOO^* \leftrightharpoons * + O_2 + H^+ + e^-$$

$$\Delta G_4 = \Delta G_{O2} - \Delta G_{HOO^*} - eU + K_b T \ln a_{H+}$$

Different intermediates are involved in each step of this reaction. As the total free energy for the OER is determined by the step which is associated with the largest free energy change, the whole free energy change in the OER can be explained in the following equation.

$$G^{OER} = \max (G_1, G_2, G_3, G_4)$$

The theoretical overpotential which is independent from the pH in solution at the standard condition can be calculated as well.

$$n(OER) = (G^{OER}/e) - 1.23V$$

If the overpotential for each step is known, the free energy diagram for different intermediate could be deduced. In order to have the smallest overpotential for OER which produces the smallest energy loss, the free energy of each step should be the same. Thus in the ideal catalyst, the free energy of OER should be 1.23eV. So the diagram for the intermediates are shown in Figure 6 a). As shown in b)-d) in Figure 6, free energy diagrams for some of the metal oxide catalysts used in the OER are not similar to that for ideal catalyst.

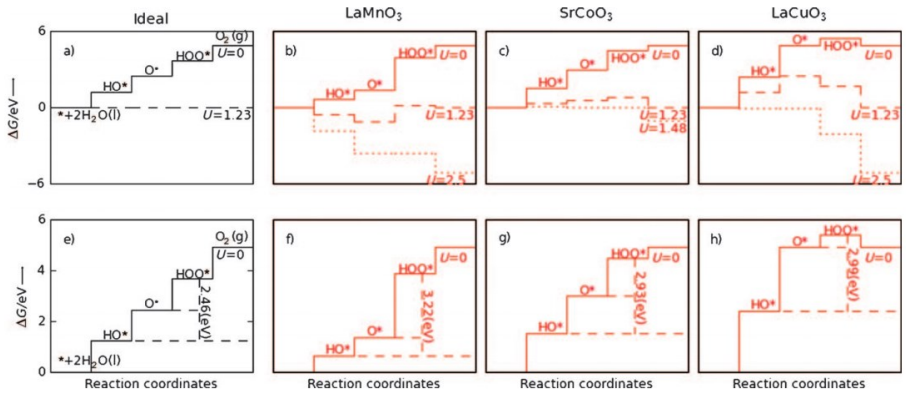

Figure 6 Free energy diagram for the ideal catalyst and metal oxide catalysts.

There is an interesting phenomenon happened to the free energy difference between HOO* and HO*. The bindings of HO* and HOO* is related to each other by the constant of about 3.2eV. This constant relationship happens because these two species usually prefer the same binding site space and the structure for these two is quite similar. ‘

Deduced from this relationship of 3.2 eV constant, overpotentail of the each oxide surface is determined by the O* adsorption energy. It is the step 2 or step 3 that are the potential determining steps.

$$G^{OER} = \max [\Delta G_2^0, \Delta G_3^0] = \max [(\Delta G_{O*}^o - \Delta G_{HO*}^o), (\Delta G_{HOO*}^o - \Delta G_{O*}^o)]$$

$$G^{OER} \approx [(\Delta G^{o}_{O*} - \Delta G^{o}_{HO*}), 3.2eV-(\Delta G^{o}_{O*} - \Delta G^{o}_{HO*})]$$

As a result, the free energy difference could be defined as the descriptor of the OER activity. So the theoretical overpotential can be calculated by the following equation.

$$n^{OER} = \{\max[(\Delta G^{o}_{O*} - \Delta G^{o}_{HO*}), 3.2eV-(\Delta G^{o}_{O*} - \Delta G^{o}_{HO*})]/e\} - 1.23V$$

Here the descriptor is defined as the free energy difference between O* and HO*.

Also, Horn's group also points out another descriptor which is named as "the near-unity occupancy of the E_g orbital of surface transition metal ions and the covalency strength in bonding to oxygen". The OER activity is related to the Oxygen bonding strength in O* species. The oxygen bonding strength will be effected by the tuning of E_g orbital since E_g orbital will participate in σ-bonding in this type of bonding. The instinct part of this descriptor is the oxygen bonding strength, and it is more complex and not straightforward. As a consequence, we use free energy difference as the descriptor to find a suitable catalyst.

1.3.3 Volcano Plot for the OER Catalysts

Plotting overpotential as a function of descriptor (free energy difference) for metal oxides. And theperovskites will give the result of the volcano-shape relationship. The relationship for these two species are shown separated in following Figure 7.

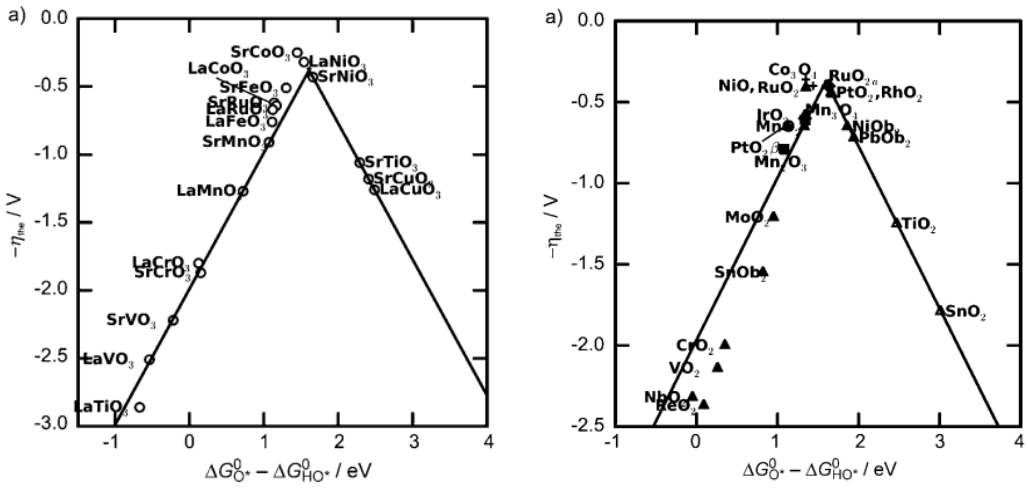

(a) (b)

Figure 7 Volcano-shape relation for different kinds of a) perovskites and b) metal oxide

This volcano shape relationship reveals that the highest catalytic activity could be obtained at a suitable value of free energy difference. The free energy difference is a function of oxygen adsorption energy, and it will increase when the oxygen bonding strength is becoming weaker. So the highest activity will show on the surfaces that bind oxygen neither too strong nor too weak. On the left side of the volcano, oxygen bond is too strong that it is hard for O* to go through chemical reaction to form HOO*. The activity indicated by operation potential (function of negative overpotential) is limited by the formation of HOO*. On the right side of the volcano, oxygen bond is too weak that it is hard for O* to form during oxidation of HO*. The reaction is limited by the oxidation of OH*. When the free energy difference for the metal oxide surface has a the value around 1.6, the overpotential is the minimum and the activity is highest. [37]

On the top of the volcano is $SrCoO_3$ which can hardly form perovskite structure. For perovskites containing transition metals like Ni, Co, Fe, Mn which are common metals in

our lives, the activities located on the left side of volcano. And the theoretical overpential of them as catalysts in the OER will increase due to the decreased value of free energy difference. In our work, perovskites containing these metals were studied. Through figure 7 b), the metal oxide can draw our attention as well. However, metallic oxide were not studied in our research, because the conductivity of the materials should be taken into consideration as well. Normally, perovskites show higher conductivity since they have smaller band gaps. For example, band gap in $LaCoO_3$ is 0.2-0.6eV compared to that in Co_3O_4 is 1.96eV. And thus, the resistance of $LaCoO_3$ is only 10 Ω*cm compared to that of Co_3O_4 which is 10000 Ω*cm. Therefore the perovskites could be good materials for OER catalysts and draw our attention.

1.4 Perovskites as catalysts for the OER

To fit the pursuit of new cost-effective and exceedingly active catalysts for energy conversion and storage, especially for electrolysis of water, perovskites have been studied extensively. As one kind of cost-efficient catalyst for OER, a range of this group of inorganic material was studies. [39-45]

1.4.1 Structure of perovskite

The perovskite is a various group of compounds having the similar crystal structure related to the mineral perovskite $CaTiO_3$. Figure 8 describes the archetypal ABO_3 crystal structure that is cubic. [46] A face-centered cubic (FCC) lattice was formed by the larger cations—A and the oxygen atoms around it. [47] The other cations which is normally marked as B, occupy octahedral sites in this FCC lattice. B cations is only surrounded by oxygen atom which is the nearest neighbors for it. These B cation occupied octahedra share corners with each other, and share faces with the dodecahedra surrounding the A cations. [48-49] This type of crystal structure is commonly called as perovskite. The chemical symbol could be written as ABX_3 and X is usually oxygen but also other large ions are also accessible. This type of structure should be the idealized cubic structure of perovskite family, for example, in $CaRbF_3$ and $SrTiO_3$. The latter can be explained as Sr^{2+} and O^{2-} ions forming a cubic close packed lattice while Ti^{4+} ions occupying the octahedral holes created by the oxygen atoms. Most kinds of perovskites are distorted and cannot described as the ideal cubic structure. The more detailed crystal structure and properties (e.g. ORR activity) vary much from each other by alternating the component

of A and B. Also it can depend on the relative amount of the different elements of A and B.

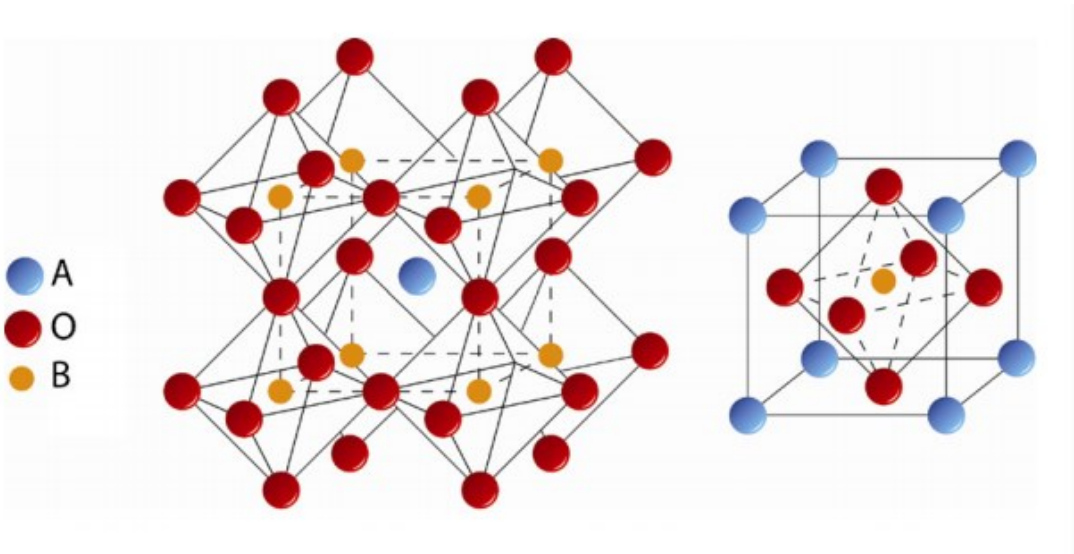

Figure 8 Cubic perovskite structure [49]

1.4.2 Perovskite for the OER

The OER with the existence of metal oxide catalysts can be elucidated into four steps. The proposed OER mechanism on perovskite transition-metal oxide catalyst is shown in the following scheme in Figure 9. [50-56]

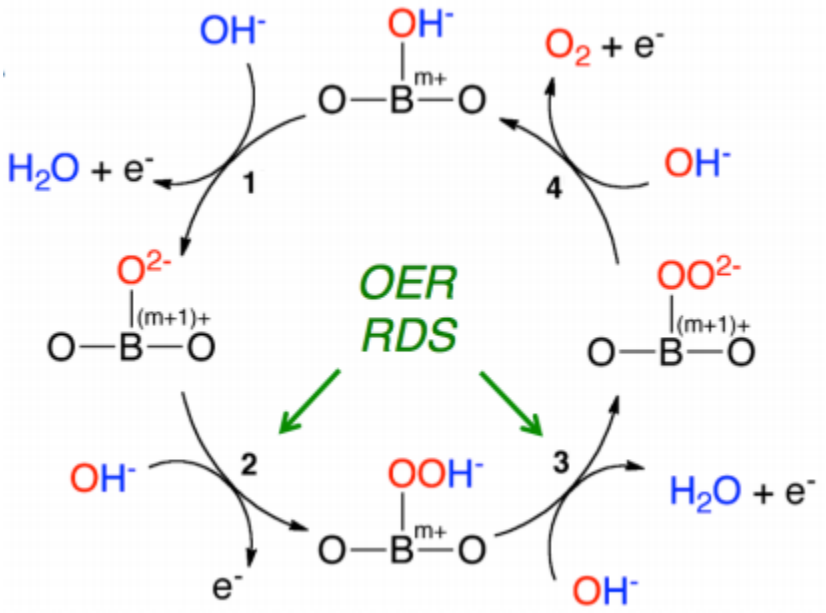

Figure 9 Proposed OER mechanism on perovskite catalysts [55]

The rate determined step (RDS) is O-O bond formation in the second step and the proton extraction of oxy-hydroxide group in the third step.

In 1984, electrocatalysis of eighteen kinds of perovskites towards the OER was studied by John O'M. [50] In their study, a plot of Tafel plot intercepts vs. the d-electrons amount of transition metal was showed. The number of electrons occupying the antibonding ortital can affect the OER catalyst activity. The larger the number was, the higher electro catalytic performance would be obtained. Also, they demonstrated that the activity of lanthanum nickel oxide catalyst is the highest.

After that, researchers studied the electrochemical performance for thin films of perovskites. One example was the characterization of thin films of $LaNiO_3$ conducted by R. N. Singh in 1994. [56] They used the spray pyrolysis method to produce perovskite thin film. The CV studies revealed the redox peak from Ni (III)/Ni (II) during oxygen

evolution in alkaline solution. And the Tafel slopes were about 40 and 65 mV/decade. In addition, they proposed that formation of the physical adsorbed H_2O_2 was involved in the rate determining steps.

Shao-Horn's group [55] reported that intrinsic OER activity can be enhanced by the near-unity occupancy of the Eg orbital of the surface metal ion with high B-site oxygen covalency. After plotting the relationship between Eg occupancy and the OER activity for perovskite of 0.8-1um, a volcano shape line similar to the Rossimeisl's study was obtained.

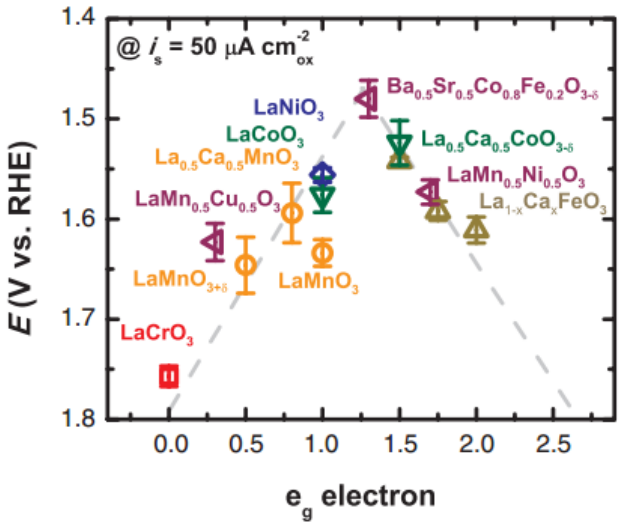

Figure 10 Relationship between the OER catalytic activities and the occupancy of the E_g-electrons of the transition metal oxide

In Figure 10, deprotonation of the oxyhydroxide (OOH-→O_2^{2-}) is proposed to be the RDS in the left side. And as for right side, formation of O-O bond might be the RDS. As a result, this relationship could be described as volcano shape and the highest OER active material should be on the top of this relationship.

These studies revealed the brief introduction to the catalyst performance of perovskites group. However, most of these recent research focused on the instinct activity of the perovskites particles of large size. And the method used in these papers to form perovskites can normally cause the significant increasing of the particle size.

Here, we aimed at synthesis of smaller size of perovskites especially nanoparticles which can obtain unusual performance. And we retested the trend of the OER catalysis activity for these perovskites particles of smaller size. In addition, same perovskites of different size was also studied.

Chapter 2 Synthesis of perovskite nanocatalysts

2.1 Sol-gel method

A sol-gel method was emplyed in the experiment. The major difference between this method and the others described in previous studies is that it will produce a gel which will play an important role in controlling the size of perovskite particles.

The gel was formed after adding of citric acid and ethylene glycol. In the acid water solution, aquo-cations are formed. For example, in the presence of citric acid, metal aquo-cations will undergo complexation and chemical controlled condensation, generating a metal-citric acid chelate. In the chelate, citric acid is bound as a coordinated ligand. By heating, the weak bounded ligands (citric acid and anion from precursor) will be oxidized and released. And remained La-transition metal part will remain to be coordinated by the oxygen in air and transform to perovskite particles.

During annealing, the temperature and the duration of calcination can be tuned. This proves be a good way to control the size of particles.

2.2 Chemical agents

$La(Ac)_3$, $Co(Ac)_2 \cdot xH_2O$, $Mn(Ac)_2 \bullet xH_2O$, $Ni(Ac)_2 \bullet xH_2O$, $Fe(Acac)_3 \bullet xH_2O$, citric acid and different types of carbon were ordered from Strem or Sigma-Aldrich company. High surface area carbon (≈900 m2/g) were purchased from Tanaka K.K. All the materials are used without further purification.

2.3 Experimental protocols

2.3.1 Synthesis of La-based nanocatalysts

Figure 11 shows a common system for sol-gel synthesis of La-based perovskite particles. The carbon and all the other chemicals involved in reaction were added into a small vial (20mL) for the formation of the gel. The precursor solution was first fully dissolved in the deionized water and mixed to the ratio of 1 to 1. Then the citric acid was added into system. The reaction vial was heated by a flat mantle (80W-115V) in 100-110 degree to evaporate the water in system. The solution was stirred by a Teflon coated magnetic bar. The speed of stirring is about 1200 rmp. Steady and mild air stream was blown into the vial to fasten the evaporation of the water. After few hours, a gel solution was formed and being heating in the furnace to get rid of the organic remainders in the system. In the following annealing, a tube furnace with nitrogen flow might be needed in some cases. Different temperature, from 600 C, 800 C to 1000 C were used for annealing for different samples.

2.3.2 Synthesis of La-based nanocatalysts with carbon support

Different types of carbon black was added into system right after solution reached homogeneous. 0.24 g carbon black was added. Sonication was used at some time to accelerate the process. A steady and mild air was blown into the vial to fasten the evaporation of the water. After 2 hours, a gel solution was formed and then heated in the furnace to get rid of the organic material in the system. In the following annealing, 400 degree for 2 hr was used to get rid of the carbon. Following with 600 degree to improve the morphology and crystallization.

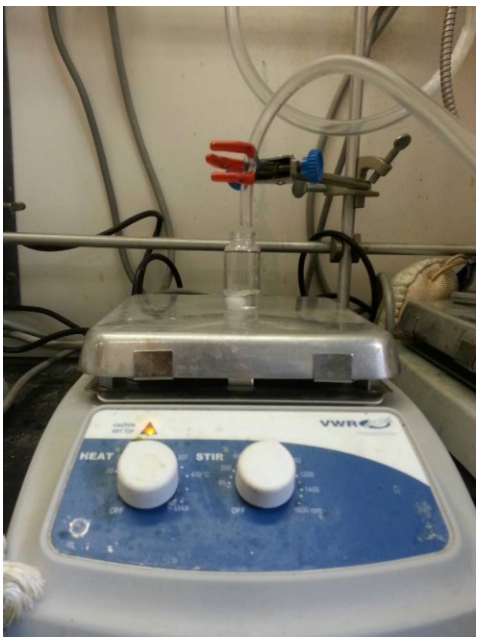

Figure 11 General setup for perovskite nanoparticles

2.3.3 Synthesis of La-based nanocatalysts with silicon template

Equal molar lanthanum nitrate and cobalt nitrate was dissolved in deionized water and ethanol to prepare the precursor. Same molar ratio of citrate acid to total amount of metal ions was added. Typically, 2 mmol lanthanum nitrate, 2 mmol cobalt nitrate, and 4 mmol citric acid were dissolved in a mixture composed of 7.5 mL of ethanol and 2.5 mL of deionized water. After stirring overnight at room temperature, solution became homogeneous, following with adding 0.5g hard template (silica). The solution was stirring for 8-10 hours at 40 degree to make it viscous, following with drying at 80 degree for 6 hours. Calcination at 500 for 4 hours was applied to decompose nitrate stuff. Same process was repeated except the precursor was reduced to half. After following

calcination, silica was removed by 2 M NaOH solution etching. After washing and drying, $LaCoO_3$ nano particles was obtained.

Chapter 3 Instruments Characterization

3.1 Instruments

3.1.1 Transmission electron microscopy (TEM)

The Integrated Imaging Center at Johns Hopkins University provided low resolution 120 kV, FEI Tecnai 12 TWIN transmission electron microscope for attaining the transmission electron microscopy (TEM) imaging. From these images, macro analysis of nanoparticle structure and morphology was studied.

Samples for TEM imagining were prepared on amorphous carbon coated copper grids (Ted Pella, Inc.). It is deposited onto that grid by adding one drop of diluted nano particle dispersion in hexane. Usually, the grids were dried in air for several minutes before test.

3.1.1 X-ray Powder Diffraction (XRD)

X-ray diffraction patterns (XRD) were measured using a PANalytical X'Pert3 Powder X-Ray Diffractometer containing a Cu Kα radiation source (λ=0.15406). This instrument was provided by Johns Hopkins Materials Science and Engineering Department.

Also, some of X-ray diffraction (XRD) patterns of powders intimately mixed with Carbon were collected on a Bruker D8 Focus instrument using monochromatic Cu Kα X-rays and an energy discriminating LynxEye detector. Powders after annealing were

immobilized onto glass slides with petroleum jelly. The instrument and the material were provided by the McQueen's Lab in Chemistry department in Johns Hopkins University.

3.2 Different types of perovskite nanoparticles

Jin Suntivich and Hubert A.[55] used the co-precipitation method to synthesize different types of perovskite particles including La-based perovskites. They used rare earth nitrate and transition-metal nitrate in a 1:1 mole ratio to form a water-based solution. For example, 1 mmol $La(NO_3)_3 \cdot 6H_2O$, 1 mmol $Co(NO_3)_2 \cdot 6H_2O$ was dissolved in deionized water. Then tetramethylammonium hydroxide was added into solution to form blue precipitate. After the sediment was collected, heat treatment at 1000 ^oC in the air was conducted. The average diameter for the synthesized particles are as following: $LaMnO_3$ 1.05um, $LaFeO_3$ 1.01um, $LaCoO_3$ 1.10um, $LaNiO_3$ 0.24 um. It was normally larger than 200nm and some of them even were larger than 1000nm.

With the concern about the super high surface area and unique properties of nanoparticles, we try to synthesize the perovskite nanoparticles. According to the sol-gel method, metal-citric acid chelate will first formed. During the calcination, the organic part will be oxidized and evaporated. The La-transition part will combine with the oxygen in atmosphere to form perovskites. The size of synthesized particles could be controlled by changing calcination temperature and duration.

In this work, different types of perovskite nanoparticles were synthesized. After evaporating the water in the original solution, gel was formed and it showed dark color corresponding to the color of metal ion. For example, the color of gel was green, pink,

yellow and red during synthesis of $LaNiO_3$, $LaCoO_3$, $LaMnO_3$, and $LaFeO_3$, respectively. As shown in the figure 12, the gel is green and transparent during synthesis of $LaNiO_3$.

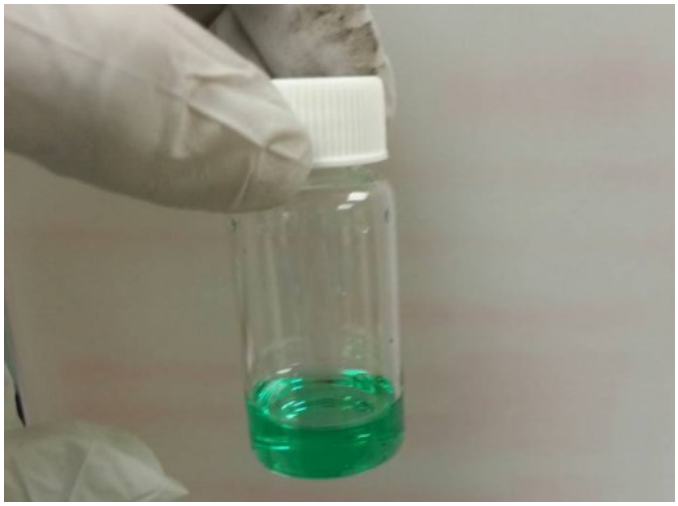

Figure 12 Picture for the gel formed during $LaNiO_3$ synthesis.

After got the gel for each metal perovskite, a step of annealing was conducted after heat-treatment in 185 degree overnight. All samples were annealed in air atmosphere at 400 degree for 1 hours and then higher temperature for 4 hours. The detail temperature and duration was shown in the following table.

$LaMO_3$	temperature	time
La_2NiO_4	1000 ^oC	4hr
$LaNiO_3$	800 ^oC	4hr
$LaCoO_3$	800 ^oC	4hr
$LaMnO_{3+\delta}$	800 ^oC	4hr
$LaMnO_3$	1000 ^oC	4hr
$LaFeO_3$	1000 ^oC	4hr

Table 1 Temperature and duration for different perovskite synthesis

3.2.1 Results of X-ray Powder Diffraction (XRD)

Powder XRD patterns of the perovskite particles (shown in the figure 13) determined the formation of perovskite structures through confirming the presence of regular group of peaks at different angles, which arises from particular set of reflections. The sharp diffraction peaks indicated good crystallinity for each species. Detail phase identification and JCPDS-PDF information from a peak matching procedure was list in the following Table 2ao. And Crystal size of each kind perovskite particles was also demonstrated since the different size crystal could influence the width of corresponding reflect peak. The smaller crystal size is, the broader the peak is. When crystal size is included in the range from 10nm to 100nm, scherrer equation can be applied to calculate the crystal size through full-width at half-maximum height (FWHM). The calculation was given in the appendix.

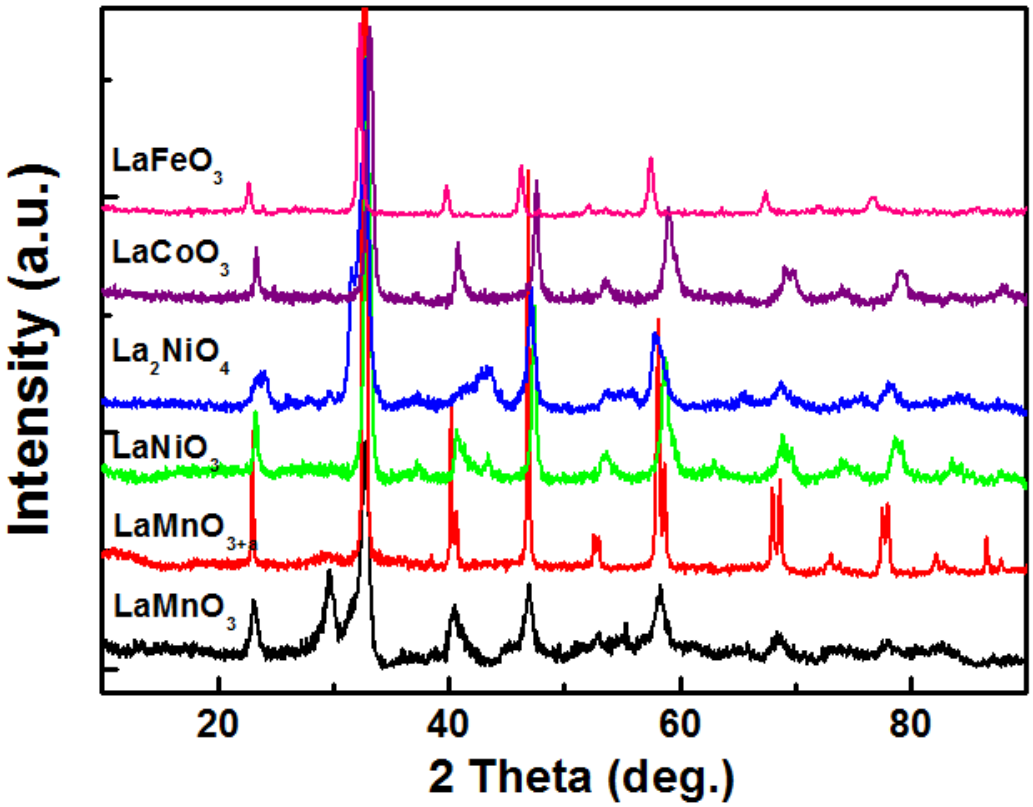

Figure 13 X-ray diffraction (XRD) patterns of La_2NiO_4, $LaNiO_3$, $LaCoO_3$, $LaMnO_{3+\delta}$, $LaMnO_3$, $LaFeO_3$

$LaMO_3$	phase	JCPDS-ICDD PDF no.	Crystal size	Space group no.
$LaCoO_3$	all	0048-0123	86.6nm	P-3c(167)
$LaNiO_3$	all	0033-0711	82.2nm	P-3m(166)
La_2NiO_4	most	0034-0314	81.1nm	I4/mmm(139)
$LaMnO_3$	all	0054-1275	75.8nm	N.A.
$LaMnO_{3+\delta}$	all	0050-0298	59.2nm	P-3c(167)
$LaFeO_3$	all	0037-1281	60.7nm	P-3m1(164)

Table 2 Detail phase identification and JCPDS-PDF information

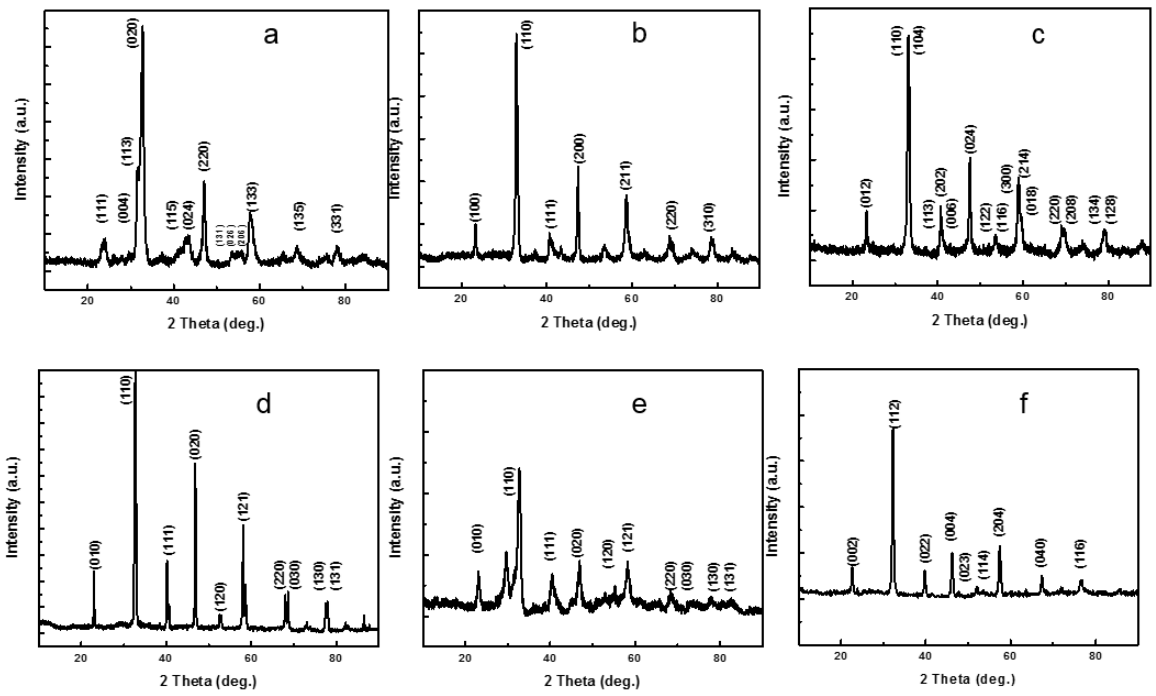

Figure 14 Detailed X-ray diffraction (XRD) patterns of a) La_2NiO_4, b) $LaNiO_3$, c) $LaCoO_3$, d) $LaMnO_{3+\delta}$, e) $LaMnO_3$, f) $LaFeO_3$.

Detailed XRD information can be found in the figure 13 and 14. The XRD pattern for each sample showed that all of them are perovskite particles and the characterized peak for them is the strongest peak at 30 degree. For La_2NiO_4 and $LaMnO_3$, the peak is not very obvious. Normally the strongest peak for these perovskite particles indicated the (110) face. All the size calculated from XRD pattern showed that they shared a similar size of 60-80nm. That demonstrated the similar surface area for them.

3.2.2 Size analysis from TEM and SEM.

The SEM studies in the following figure 15 show that all the samples are quite uniform and sphere like. The surface morphologies are kind of different for each perovskite. Most of the sample were formed by aggregation. Small domains of approximately 10-30nm was formed while these domains further aggregated to become large particles which is normally 200-300nm. However, for $LaNiO_3$, the size was smaller even though the calcination for it was the same as others. For $LaCoO_3$, the aggregated particles formed a unique network connection which might mislead in calculation of size from geometry.

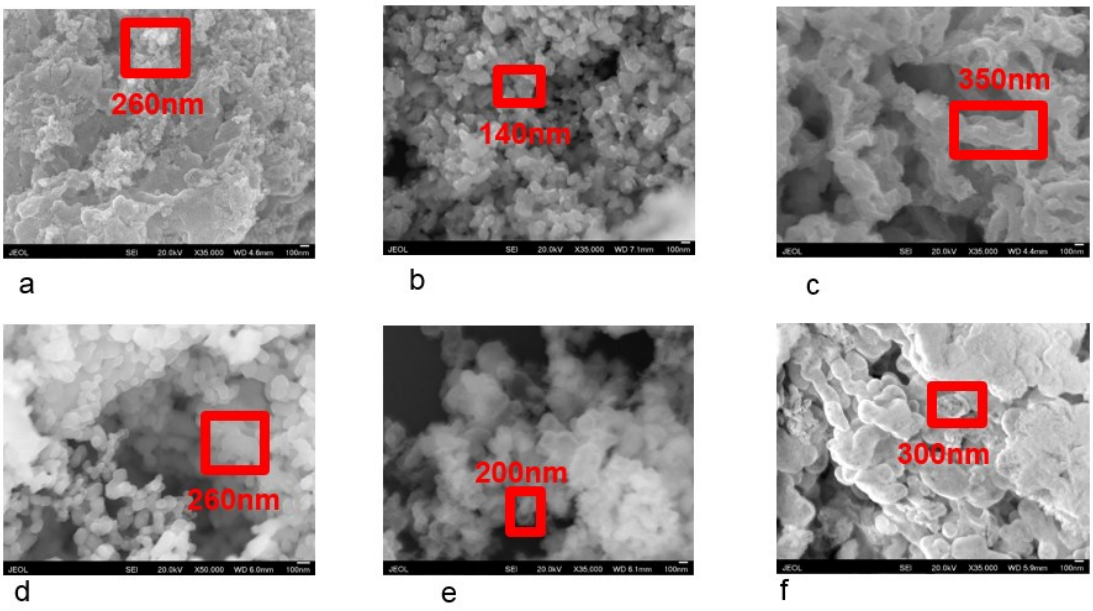

Figure 15 SEM images of a) La_2NiO_4, b) $LaNiO_3$, c) $LaCoO_3$, d) $LaMnO_{3+\delta}$, e) $LaMnO_3$, f) $LaFeO_3$.

The TEM imagines in figure 16 show that the average size of small domain is about 30-80 nm. And the small domains formed aggregated particles of average 300 nm. However, TEM gave the inside look that aggregated particles formed from small domains were hollow structure. The S&TEM study confirmed similarity in the size of these samples. Compared to normal size of 1000 nm for perovskite, the particles here is really small.

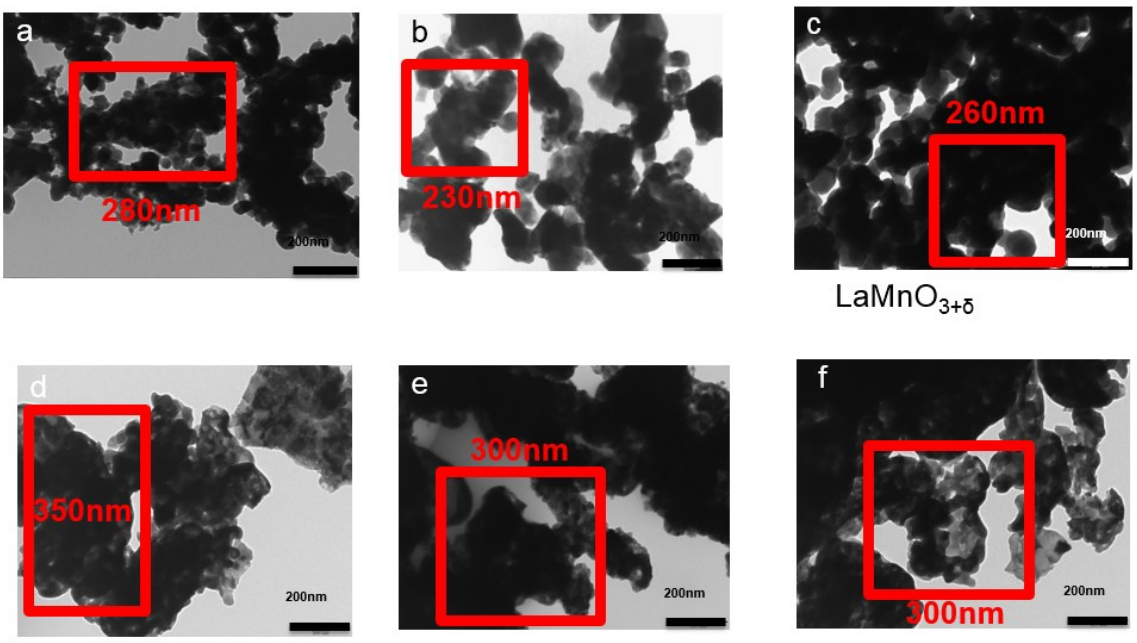

Figure 16 TEM images of a) La_2NiO_4, b) $LaNiO_3$, c) $LaCoO_3$, d) $LaMnO_{3+\delta}$, e) $LaMnO_3$, f) $LaFeO_3$.

3.3 $LaCoO_3$ nanoparticles of different sizes synthesized with carbon support

To control the size of $LaCoO_3$ particles, different types of Carbon were added into the precursor solution before evaporating water. For example, Tanaka Carbon, active carbon and acetylene carbon. After the gel was formed, calcination in 400 degree for 1 hour will allow $LaCoO_3$ to form with the protect effect of carbon. After that, 600 degree was used to get rid of the carbon and form the crystal structure of $LaCoO_3$. XRD patterns shown in 错误!未找到引用源。 confirm that $LaCoO_3$ is produced after heat treatment while the compound is no single phase. This might happen because some La-based perovskites will react with carbon at high temperature during annealing.

Scherrer equation: $D= K\lambda / B\cos\theta$ was introduced to calculate the size of crystallites. D is the means size of the ordered domains and it is always smaller or equal to the real size. This equation is accurate when D is larger than 1nm and smaller than 100nm. K is the shape factor while it is 0.89 for sphere particles in my case. λ is the wavelength of X-ray. B is the FWHM (line broadening at half the maximum intensity). And the θ is the angle for corresponding peak. In my calculation, the FWHM and the angel from the strongest peak were used to calculate.

Though the XRD peak showed different intensity for different particles as showed in the figure 17, the FWHM was relatively similar to each other indicating the size of ordered domain was similar. Size for each sample were summarized in the following Table 3. The calculation of the size from XRD was attached.

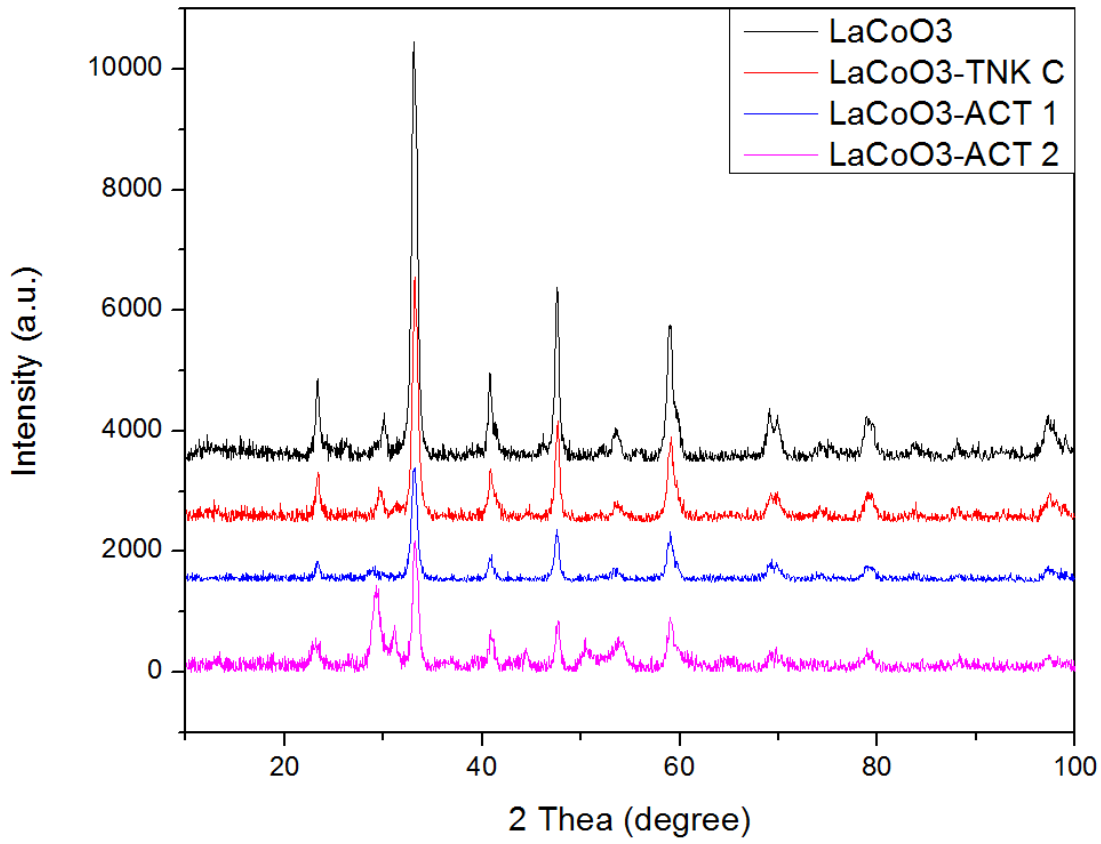

Figure 17 Comparison of XRD patterns for $LaCoO_3$ a) without carbon b) with TANAKA carbon c) with active carbon 1:1 in mass d) with active carbon 1:2 in mass

Type (nm)	$LaCoO_3$ 20140206T1	$LaCoO_3$-Tk C 20140109T1	$LaCoO_3$-Active C 20140109T1(1:1)	$LaCoO_3$-Active C 20140206T1(1:2)
Hand	14.16	13.35	14.11	14.06
Jade	14.00	14.30	14.50	15.20

Table 3 Comparison of different sample of $LaCoO_3$ nanoparticles

In order to explore the morphology of the $LaCoO_3$ nanoparticles and reveal the morphological size for each sample, all the samples were studied by TEM. Figure 18 shows agglomerates whose size ranges from 30 nm-100nm for $LaCoO_3$ and $LaCoO_3$ with

Tanaka Carbon (TNK C) while 10-30nm for $LaCoO_3$ with active in ratio of 1:1 and 1:2 in mass. However, the broad size distribution was also observed.

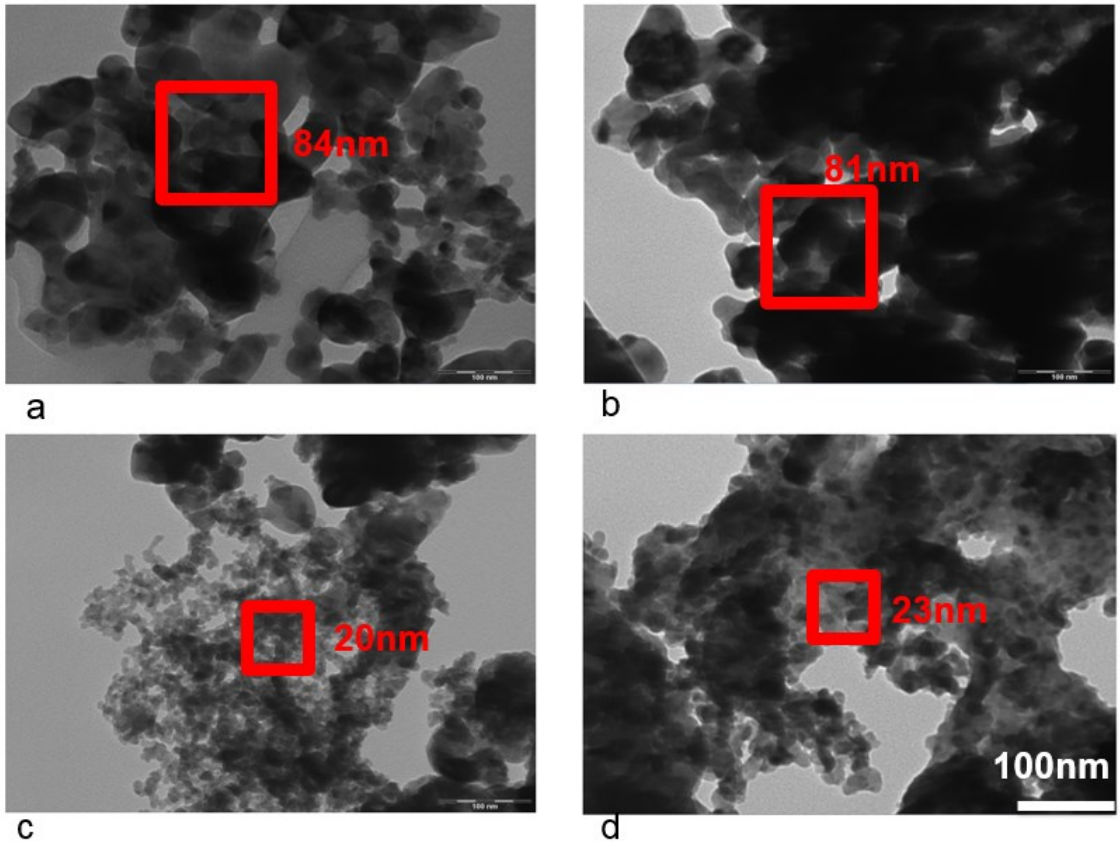

Figure 18 TEM for different types of $LaCoO_3$ nanoparticles synthesized with carbon (Scale bar=100nm)

Type (nm)	$LaCoO_3$ 20140206T1	$LaCoO_3$-Tk C 20140109T1	$LaCoO_3$-Active C 20140109T1(1:1)	$LaCoO_3$-Active C 20140206T1(1:2)
XRD	14.16nm	13.35nm	14.11	14.06
TEM	30-60nm	22-30nm	15-20	9-16

Table 4 Size comparison of different types of $LaCoO_3$ nanoparticles.

Combining the TEM, SEM and XRD for these samples, the carbon cannot help to decrease the size of $LaCoO_3$ particles. And the small domains of samples synthesized with active carbon is smaller under TEM. Also, there were some impurity phase in them and this would influence the E-chem test and then the activities shown in the E-chem would be unreliable.

3.4 $LaCoO_3$ nanoparticles of different sizes

To make smaller $LaCoO_3$ nano particles, silica as the hard template was added during production of precursor. Meanwhile to make larger $LaCoO_3$ particles, the sol-gel method with tuning the temperature during calcination was applied.

The mechanism for silica template method was explained in many papers. After adding the silica template, the perovskite particles will form inside of the template and the size is controlled as the size of space inside template. After the calcination, silica was washed away by alkaline solution and this process was much cleaner and did no harm to the catalyst compared with wash method with acid.

After annealing, XRD proved that $LaCoO_3$ same phase was produced from silica template method and the crystal size is 14.5nm calculated from scherry equation. For the other samples from sol-gel method, the single $LaCoO_3$ phase was also formed. The strongest double peak for this type of perovskite was around 30 degree. And these two peaks indicated the (110) and (104) crystal phase. The XRD pattern was shown in the Figure 19. It is obvious that the strongest peak of sample synthesized with silica is broader than others.

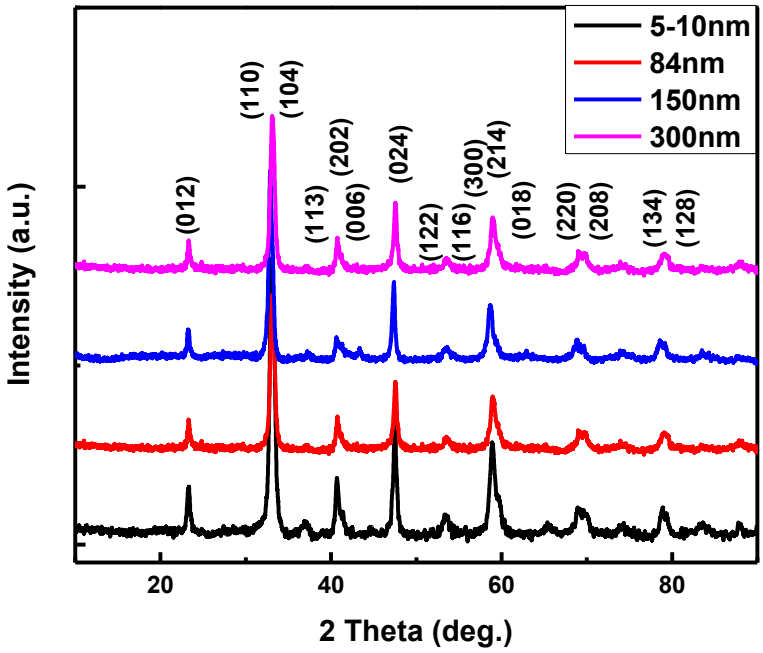

Figure 19 X-ray diffraction (XRD) patterns of $LaCoO_3$ with different size

The following SEM study in Figure 20 confirmed that the size of small lattice in the product was about 5-6nm which is corresponding to the XRD result. The SEM imagine for $LaCoO_3$ synthesized with silica template and $LaCoO_3$ synthesized in lowest temperature is hard to see the morphology. However for the samples conducted with the higher temperature and longer time, SEM was enough. 800 degree for 6 hours gave the 150nm particles and 900 degree for 6 hours gave the 300nm particles.

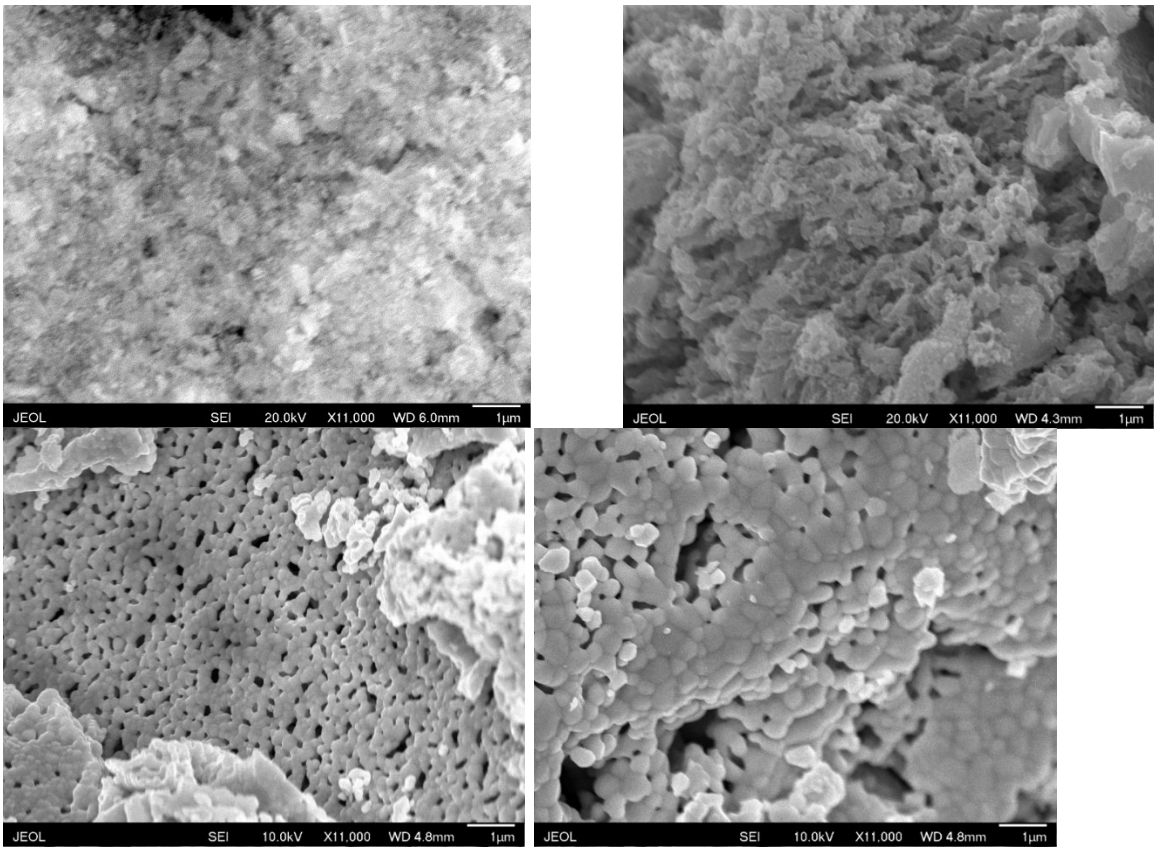

Figure 20 SEM imagines of $LaCoO_3$ with different size

Since the SEM could not show the detail information especially the size of small domains, TEM was applied. Figure 21 shows the LaCoO3 synthesized with silica hard template is nanoporous and the size of holes inside it was normally 5-10nm. For the sample with sol-gel method with calcination under 600 degree for 4 hours, the size was about 84nm in average.

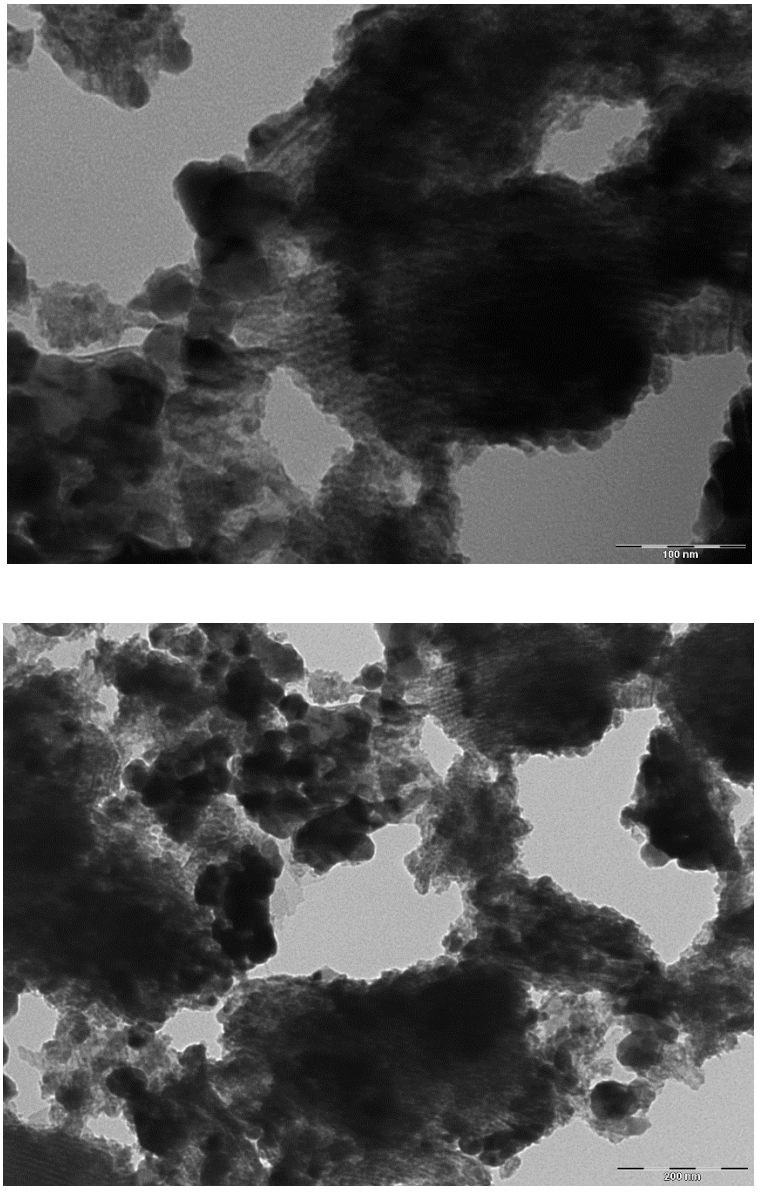

Figure 21 TEM of $LaCoO_3$ with silica

Through changing the temperature and duration in sol-gel method and through a new synthesis with silica template, $LaCoO_3$ with different size was formed and characterized by XRD, TEM and SEM.

Chapter 4 Electrochemical Studies

After annealing, about 0.05 g of the as-synthesized perovskite NPs solid was placed in a small vial. Deion water was added to make a 1g/L solution.

The electrocatalytic activities of perovskite catalysts were measured with a rotational disk electrode (RDE, 5 mm diameter) setup (Pine Inst. Co.) in a three compartment electrochemical cell (ASG Co.) and an Autolab 302 potentiostat (Metrohm). A saturated Ag/AgCl electrode and a platium wire were used as reference and counter electrodes respectively, in a 0.1 M KOH electrolyte solution. Perovskite samples were prepared in a dispensed solution with sonication over one hour. 20 μL of the as-prepared solution was deposited on the RDE surface and waited for 10 minutes to dry. All electrochemical data was collected following the first potential cycles. All potentials discussed in the results section are given against the reversible hydrogen electrode (RHE).

4.1 Different types of perovskite nanoparticles

Cyclic voltammetry was conducted representing the OER in 0.1 M KOH using a thin film of $LaMO_3$ nanoparticles deposited on the rotating disk working electrode, which rotated at 1600 rpm during the experiment. After running the electro chemical tests for all the samples, $LaMO_3$ (M=Ni, Co, Fe, Mn) showed an enhanced activity in the order of $LaFeO_3$, $LaMnO_3$, $LaMnO_{3+\delta}$, $LaCoO_3$, $LaNiO_3$, La_2NiO_4. Figure 23 shows the different values of the mass normalized current for different perovskites when the potential was 1.7 V vs RHE. The error bar stands for at least 3 times of scan for each sample. The

average value of the current for La_2NiO_4 is the highest, which is about 10 A/g. The current value of $LaNiO_3$ is quite similar to that of La_2NiO_4. The range of error bar even covers the same range. While for $LaCoO_3$, the current value is more stable around 7 A/g during the different scans. Following that is OER current of $LaMnO_{3+\delta}$ which is about 5 A/g. For $LaFeO_3$ and $LaMnO_3$, both of them shows low current around 1.75 A/g.

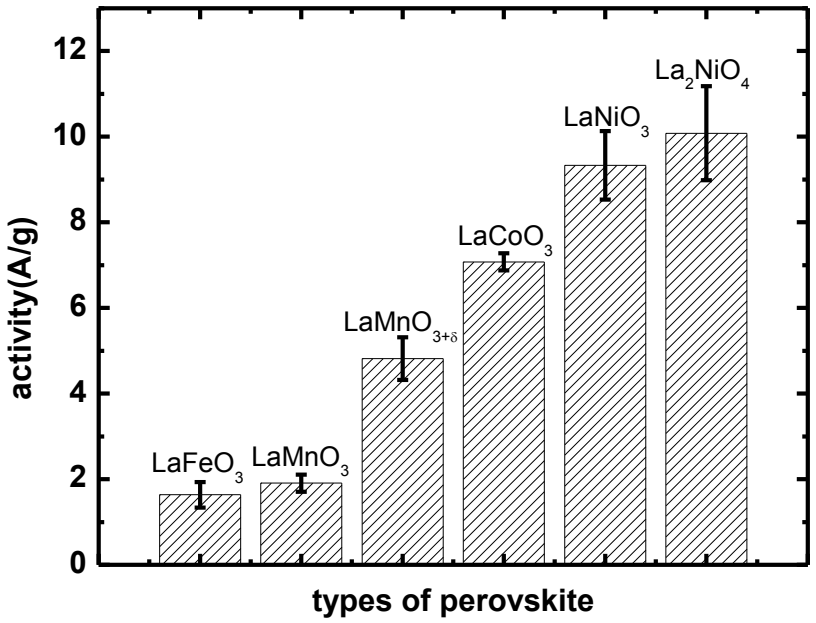

Figure 22 E-chem results of La_2NiO_4, $LaNiO_3$, $LaCoO_3$, $LaMnO_{3+\delta}$, $LaMnO_3$, $LaFeO_3$

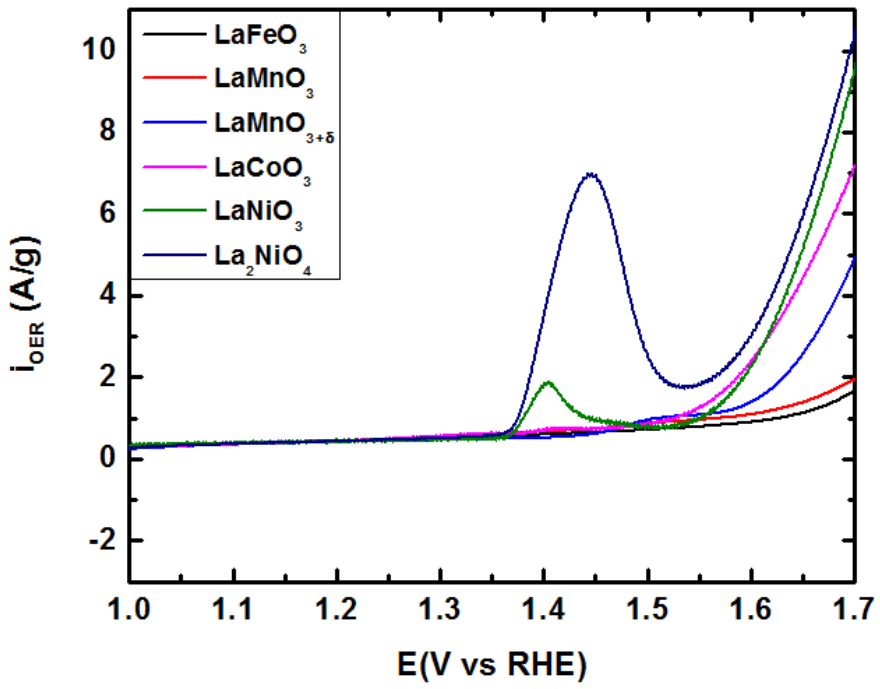

Figure 23 OER current of La_2NiO_4, $LaNiO_3$, $LaCoO_3$, $LaMnO_{3+\delta}$, $LaMnO_3$, $LaFeO_3$

The SEM and TEM elucidated that the surface area of perovskite particles was hard to measure through geometry method. While the XRD confirmed the similar crystal sizes for these perovskite particles. As a result, the OER current obtained from E-chem test was normalized by mass instead of surface area. By plotting the data close enough to the average values in figure 22, the mass normalized OER current changing with increasing potential was demonstrated. It is indicated from mass normalized current that the trend of the OER activities for perovskite was as following: La_2NiO_4 > $LaNiO_3$ > $LaCoO_3$ > $LaMnO_{3+\delta}$ > $LaMnO_3$ > $LaFeO_3$. The fact that the current changing with increasing potential for $LaMnO_3$ and $LaFeO_3$ is almost zero indicated that they are not active towards the OER. The current of $LaCoO_3$, $LaMnO_{3+\delta}$ is enhanced significantly when the potential is about 1.5 V vs RHE. Among all the four perovskites showing high activity towards OER, the OER current values of Ni-containing perovskites are the highest. In the

previous research, $LaNiO_3$ is thought to be the best catalyst towards OER among all the La-based perovskites. [62] However, same to the result in previous studies, there is a redox peak around 1.4 V vs RHE for Ni-containing perovskites. This redox peak is caused by Ni^{2+}/Ni^{3+} conversion.

To study the stabilities of these perovskites, amperometry and gavolnonstat study were conducted and the duration was set as three minutes at first. In Figure 24, the voltage was set as a constant value of 1.7 V vs RHE for amperometry study. And the current decreased slightly and could be ignored. In figure 25, the current was set as 4 A/g for galvanostat study. In the beginning, all the potentials of these samples showed the similar values to corresponding potential of during cyclic voltammetry study and then kept constant in three minutes. Both of the studies confirmed the same activity trend for different types of perovskite nanocatalysts. And the constant current indicated that these perovskite particles were relatively stable in that short time period. Compared with the galvanostat study in Horn's paper, similar stability of these samples are confirmed.

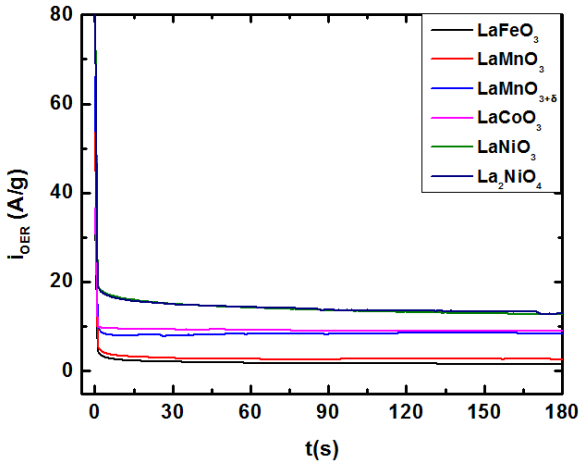

Figure 24 Amperometry studies of the OER for different perovskite catalysts.

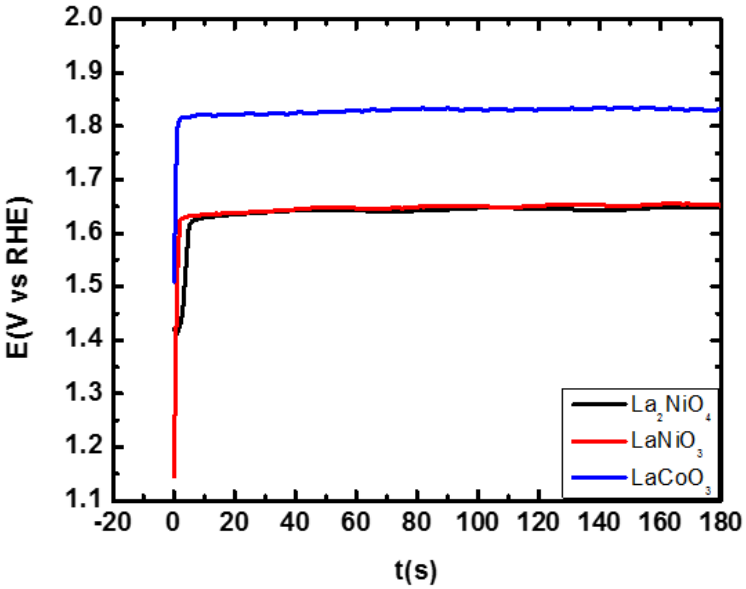

Figure 25 Short-time (galvanostat) studies of the OER current for different perovskite catalysts.

Also the time dependent OER current of $LaNiO_3$ and $LaCoO_3$ for longer duration (1 hour) was studied. Through Figure 26, the stability of them is relatively good.

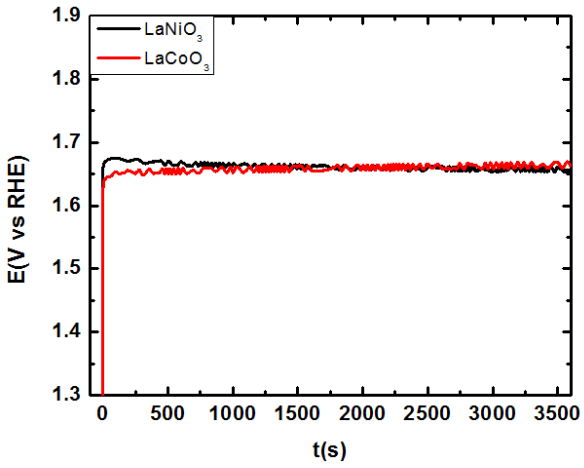

Figure 26 Long-term stability revealed by elongated galvanostatic studies of the OER for $LaNiO_3$ and $LaCoO_3$.

To understand the trend of activities towards the OER for different perovskites, the relationship between descriptor and the current values when the potential is 1.7 V vs RHE is plotted in figure 27. The descriptor of the x parameter is the free energy difference of HO* and O*. It is also the descriptor we use in this work. For transition metal perovskites we choose in this work, the relationship between descriptor and negative theoretical overpotential is a linear function and it is located on the left side of the volcano shape discussed in the introduction. As a result, when the free energy difference increases, the overpotential decreases. This means that the catalyst will have a stronger activity towards the OER when the descriptor for it is larger than the transition metal perovskites discussed in this work (Mn, Fe, Co, Ni). However, from figure 27, the Mn, Ni and Co compounds indicate a linear relationship while $LaFeO_3$ is not active towards the OER as the descriptor predicts, which is also demonstrated by Horn's group. And the reason is still unclear. If we try to find the value of free energy difference for $LaMnO_3$, the value should be larger than that for $LaMnO_{3+\delta}$. Since the $LaMnO_{3+\delta}$ is formed from $LaMnO_3$, combining more oxygen during annealing, it would have more oxygen occupancy and thus the oxygen bond is weaker during OER. So the value of descriptor of $LaMnO_{3+\delta}$ is larger. For the case of La_2NiO_4, the current value is similar (error bars cover similar range) when the potential is 1.7 V vs RHE，thus it is hard to determine which one has a larger value of descriptor.

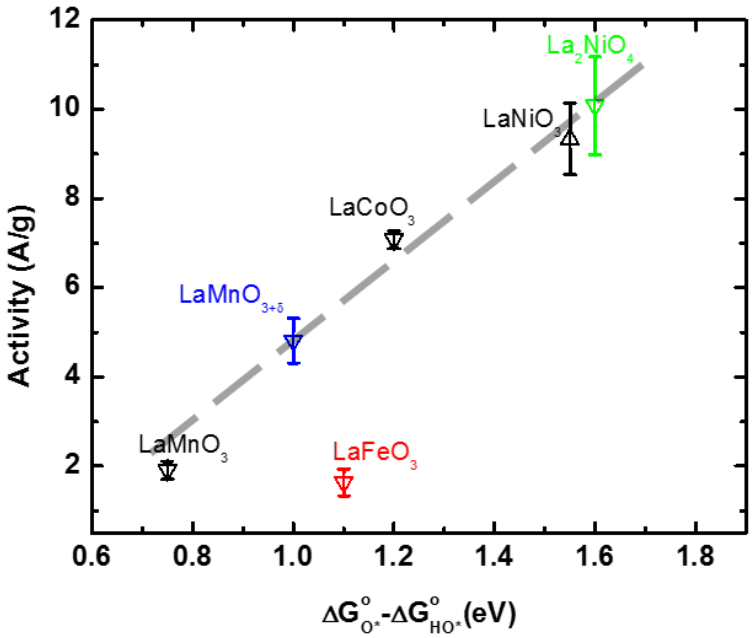

Figure 27 OER current (potential at 1.7 V vs RHE) related to free energy difference.

The relationship between the other descriptor used in Horn's group is also plotted. The descriptor they use indicates that the near-unity occupancy of the E_g orbital of transition metal ions on surface and the high covalency in oxygen bonding will increase the OER activity of perovskite catalyst. As shown in the figure 28, a linear relationship was also obtained.

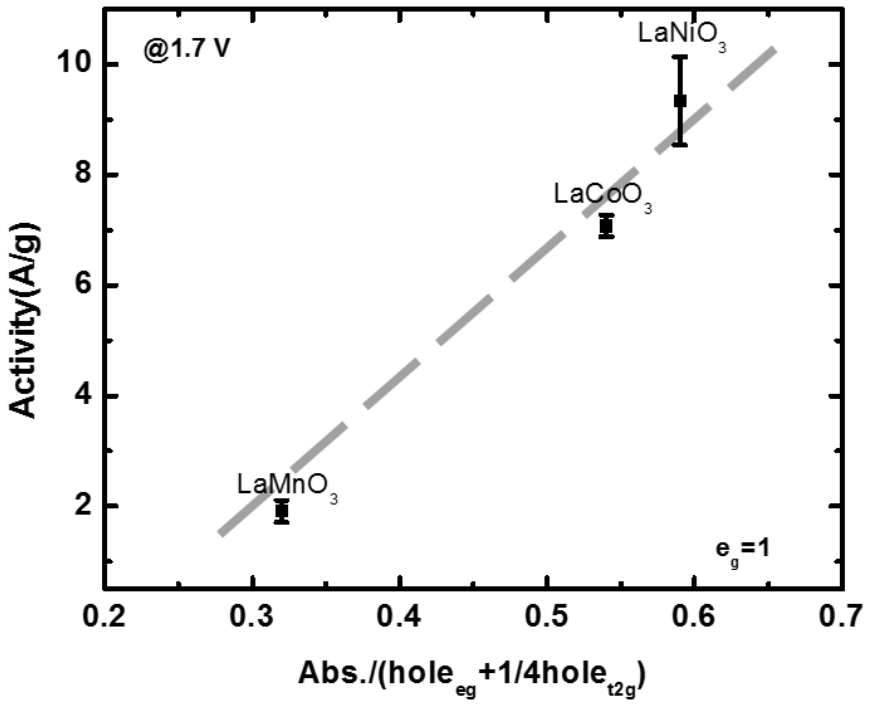

Figure 28 OER current (potential at 1.7 V vs RHE) related to metal-oxide covalence.

Additional OER current study in different range of potential is listed in the following figure 29.

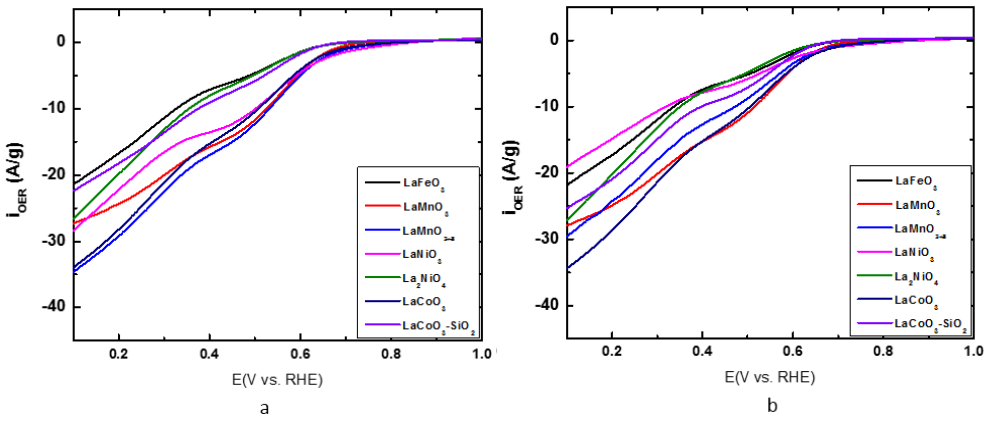

Figure 29 OER current of La_2NiO_4, $LaNiO_3$, $LaCoO_3$, $LaMnO_{3+\delta}$, $LaMnO_3$, $LaFeO_3$ in the range of a) 1.1 V to 1.7 V vs RHE, b) 1.3 V to 1.7 V vs RHE

To understand the redox peak round 1.5 V during CV scans of Ni-containing perovskite, the first scan and second CV scan for Ni-containing perovskites were plotted in below figure 30. The redox peak were unaffected by the repetitive potential steps, which was corresponded to the redox couple Ni(III)-Ni(II). And the La_2NiO_4 have more Ni(II) on catalyst surface which will go through oxidation and this can give stronger peaks.

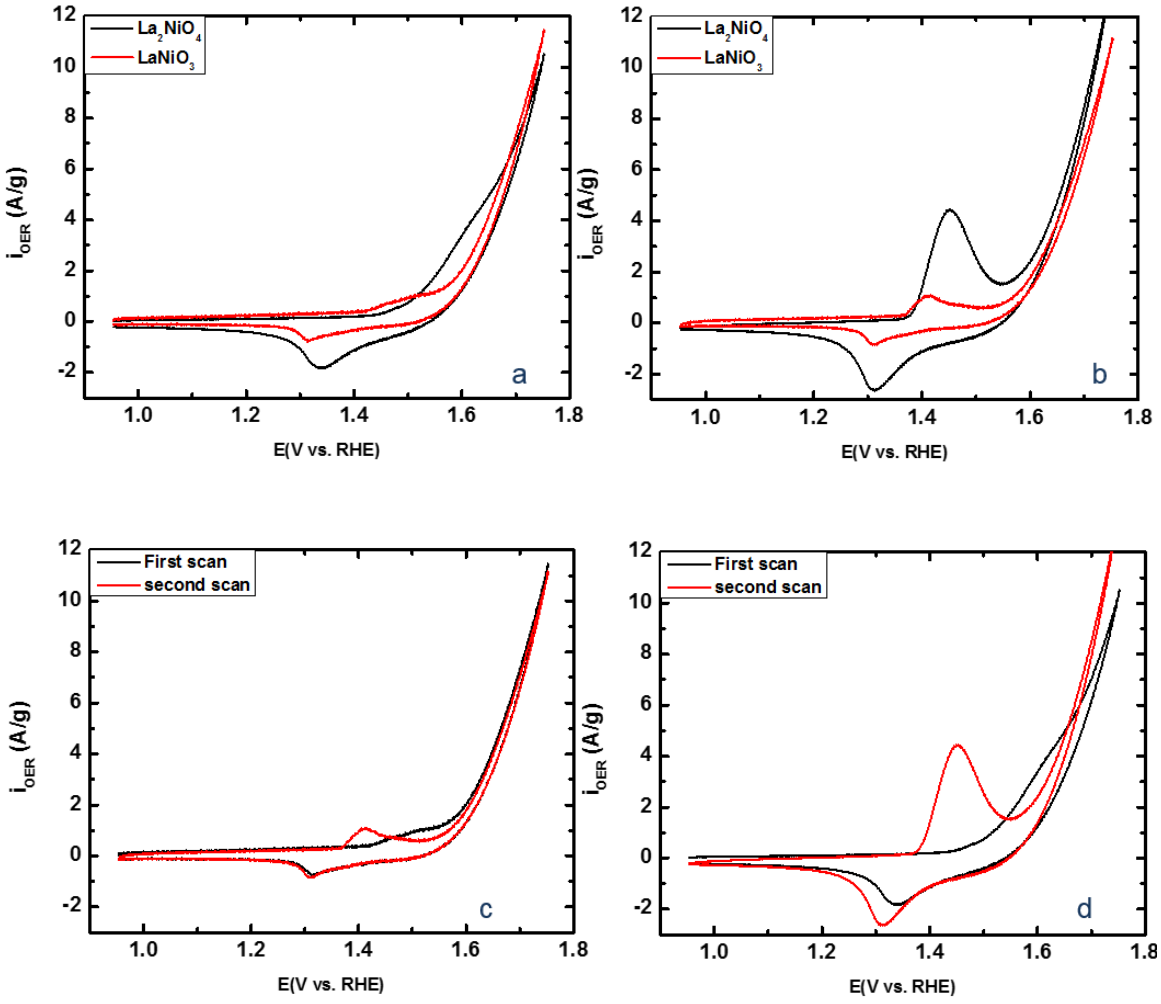

Figure 30 Cyclic Voltammetry for a) first scan of the two Ni perovskites, b) second scan of the two Ni perovskites, c) first and second scan of $LaNiO_3$, d) first and second scan of La_2NiO_4

4.2 Different size of $LaCoO_3$ with carbon support

The addition of carbon before the formation of gel was found to affect the size of $LaCoO_3$ nanoparticles. Due to the size change along with the remaining carbon in the catalysts, the scan of cyclic voltammetry was strongly affected. As shown in figure 31, 32 and 33, they were complex and unreliable. Since there was impurity phase in the sample testified by XRD, this method was replaced by a new synthesis method in the next chapter.

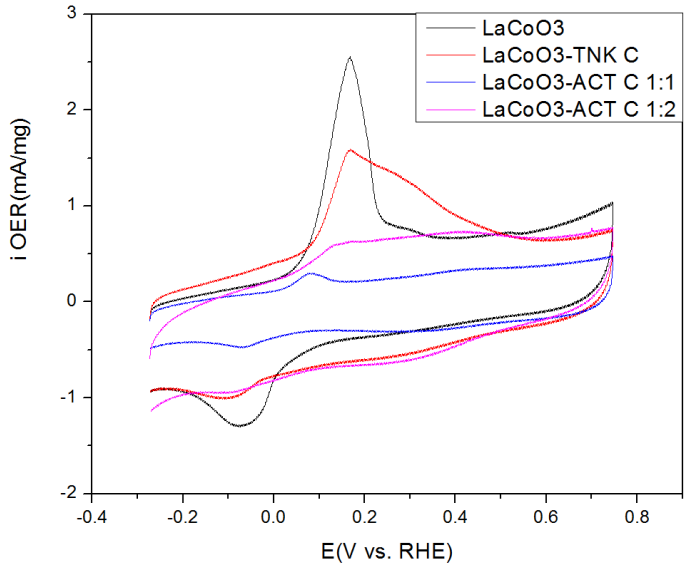

Figure 31 Different cyclic voltammetry scans for perovskite/Carbon composite electrodes in Argon-purged 0.1M $HClO_4$ at $50mVs^{-1}$

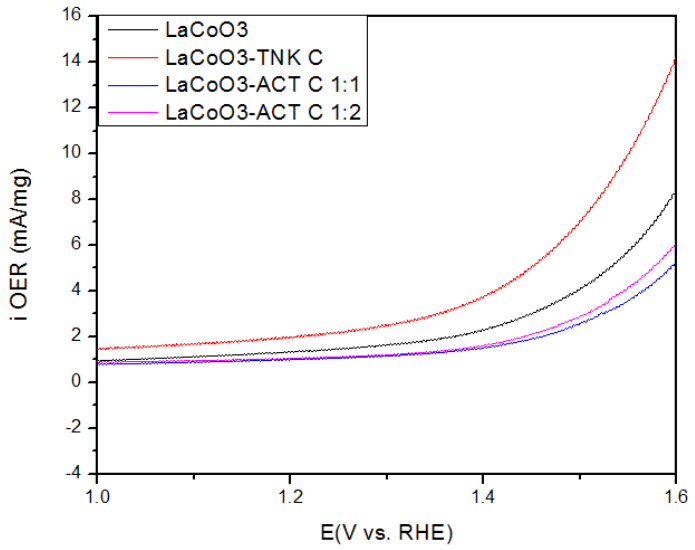

(a)

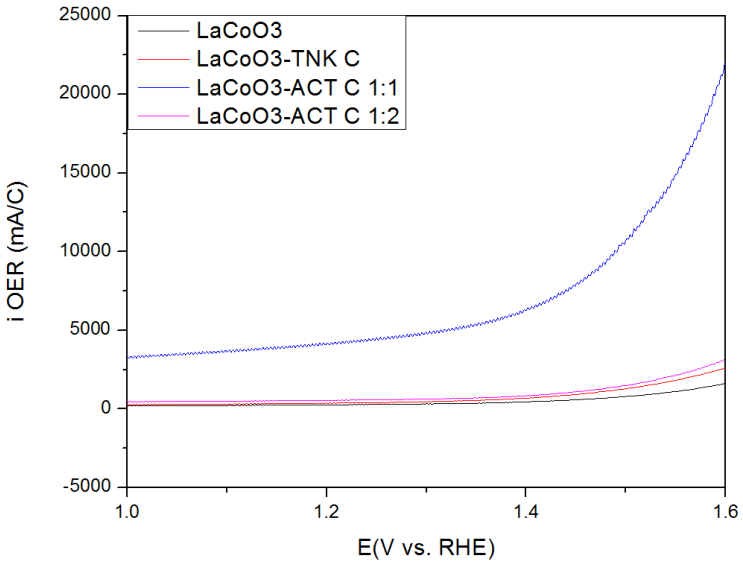

(b)

Figure 32 OER current of different types of $LaCoO_3$ synthesized with carbon in the range of a) 1.3 V to 1.8 V (vs RHE) b) 1.5 V to 1.8 V (vs RHE)

4.3 Different size of $LaCoO_3$

Figure 33 a) shows the mass normalized current for $LaCoO_3$ of different sizes when the potential was 1.7 V vs RHE. The $LaCoO_3$ of 84 nm shows the highest mass normalized OER current which is 6.4 A/g. The OER current of nanoporous $LaCoO_3$ is around 4 A/g which is the second highest. The $LaCoO_3$ of 150 nm and 300 nm shows similar low current value which is around 2 A/g. The error bars in each type of $LaCoO_3$ stand for at least three scans and at least two electrochemical samples for each $LaCoO_3$ sample.

The figure 33 b) is obtained from the group of data which is close enough to the middle of the error bars which represents the average values. By calculating the mass normalized current in paper from Shao-Horn's group, the mass normalized current for same material of 1 um is about 2.2 A/g. The current for $LaCoO_3$ samples of 84 nm we got in this work is twice higher than current reported in their paper. It is confirmed that the nanoparticles can be better catalysts towards the OER due to their high surface area and unique structures.

Through TEM, SEM and XRD, the samples of 84 nm, 150 nm and 300 nm shared a similar sphere structure. The E-chem study shows that the current increases when the size is getting smaller. This confirms that the control of size can be one method to improve the catalyst performance. For the samples synthesized with silica template, they were nanoporous particles and the size of holes inside them was about 8 nm. As a result, the size of it could be the smallest and that sample should show the highest activity towards

the OER. However, the actual mass normalized current of it was even lower than the 84nm sample. To understand this phenomenon, the current density was used here.

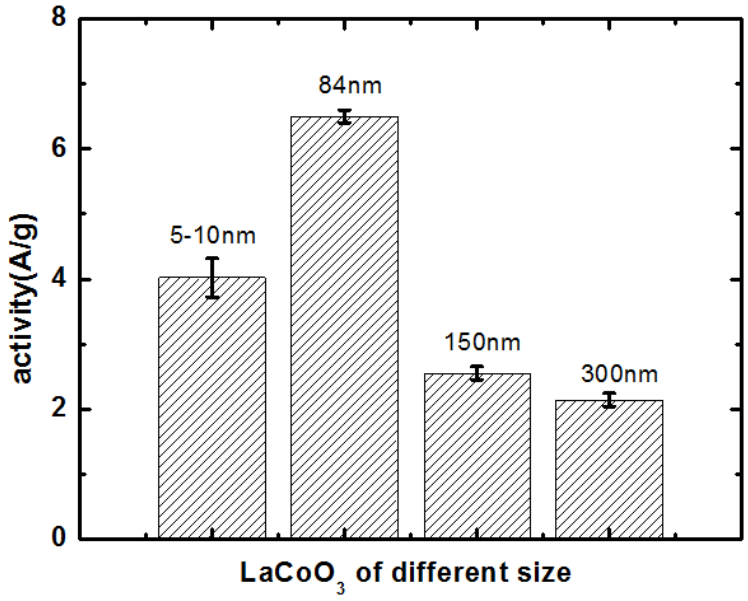

(a)

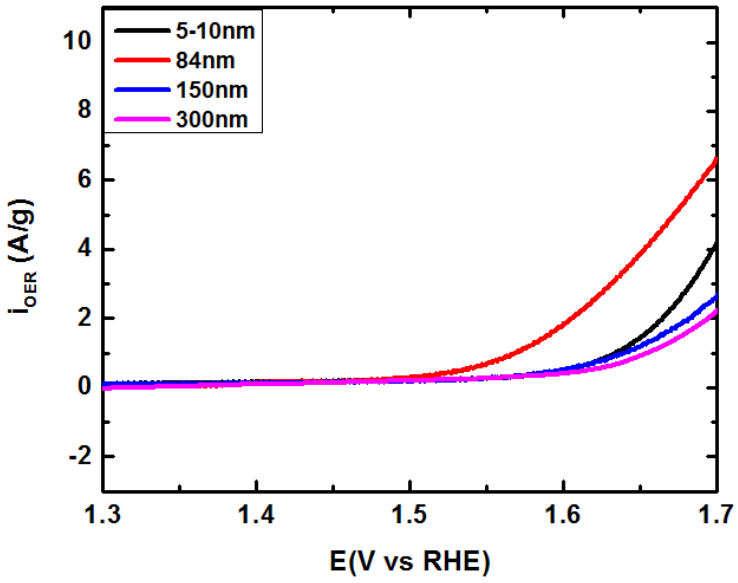

(b)

Figure 33 a) Mass normalized current for $LaCoO_3$ of different size when the potential is about 1.7 V vs RHE, b) OER current of $LaCoO_3$ of different size

To calculate the current density, the surface area for each sample was calculated through SEM, TEM and XRD. After normalization from surface area in geometry, the relationship between overpotential and current density was obtained. The slope for samples synthesized without silica is about 160-200 mV/decade. The value of slope for the 8 nm sample is only 111 mV/decade, which indicated that it is the best catalyst. It is because that the overpotential will raise slower if the current density is increasing when using this material for the catalyst in the OER. Since the overpotential is the energy loss during OER, the smaller slope indicates a better catalysis performance.

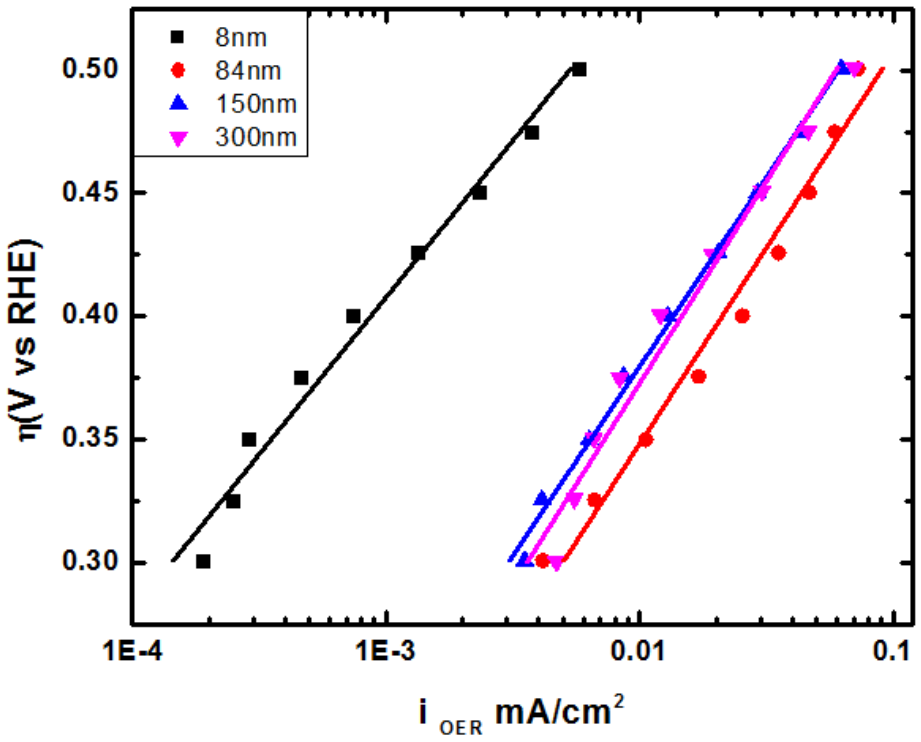

Figure 34 Tafel slope for the $LaCoO_3$ of different size, overpotential vs OER current density

The nanoporous $LaCoO_3$ which owned the highest intrinsic activity (smallest Tafel slope) towards the OER shows lower mass activity within the overpotential range shown in Figure 33 b). This phenomenon might happen due to the unique structure of nanoporous particles. As shown in Figure 35, it is a porous structure with numerous holes inside it，which means that the size of 8 nm is actually the size of holes. Inside of the particle, the OER is limited by mass transportation of hydroxyl ions. The active surface could be the surface of aggregated particles which is normally 228nm through TEM. This might cause the missing of inside active spots. As a result, it shows normal activity. The high instinct activity might be caused by two reasons. One reason is that the active spots are increased significantly and the other reason is that it contains more dangling bonds which can adsorb more hydroxyl ions and thus improve the activity.

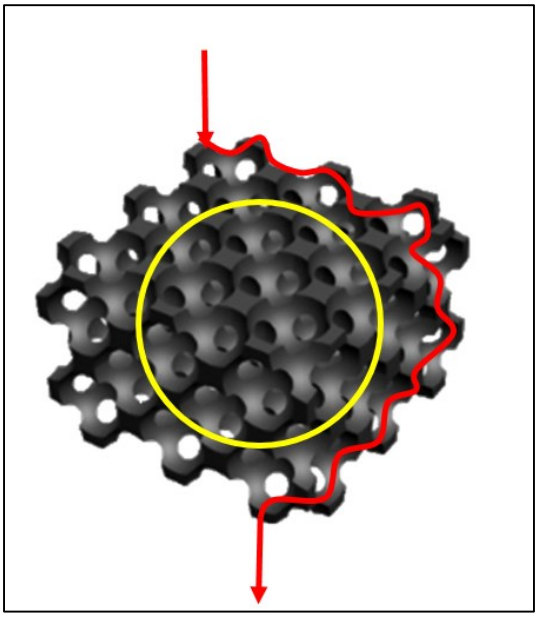

Figure 35 Structure of nanoporous $LaCoO_3$

Chapter 5 Conclusion and Future work

In this work, different types of perovskites nanocatalysts were synthesized through sol-gel method. The sizes of them were in the range from 5 to 300 nm through SEM and TEM. The similar crystal size of these perovskites was confirmed by XRD. The electrocatalytic performance towards the OER in alkaline solution of these perovskite was studied by a three-electrode electrochemical cell. The mass activity of them follows the trend: La_2NiO_4> $LaNiO_3$>$LaCoO_3$>$LaMnO_{3+\delta}$>$LaMnO_3$>$LaFeO_3$. Since the Ni-perovskite showed interesting redox peaks due to Ni^{2+}/Ni^{3+} conversion which might cause difficulty in size dependence study, $LaCoO_3$ was picked to study the size effect towards the OER activity. The smaller the size of sample was, the higher mass activity it would show. The nanoporous $LaCoO_3$ with holes of 8 nm inside was synthesized with silica template. And by Tafel slope analysis, its highest activity towards the OER was confirmed.

Since the instinct activity of nanoporous $LaCoO_3$ towards the OER was highest, it did not show the highest mass activity when the potential was not high enough. This phenomenon was caused by the structure of $LaCoO_3$ itself. Some active spots inside the structure was not active due to the limitation set by mass transportation of hydroxyl ions. To solve this problem, a new synthesis method was needed. The synthesis method should be able to keep the small size of $LaCoO_3$ and change the structure of it. As a result, $LaCoO_3$ was synthesized inside a nanoporous gold electrode. This might be a method to keep the size smaller than porous size which is 20nm and make the inside spots active in the meanwhile.

Appendix

Jade method, BG, Find peaks, Fit all peaks, Size report

$$d = \frac{K\lambda}{(FWDH) * \cos(2\theta/2)}$$

The particles synthesized from sol-gel method showed sphere morphology so it is reasonable to assume that all particles were spheres. And that gives the value for K.

K=0.89

E.g.

For active carbon1:2

Size D=0.89*0.154056(nm)/([3.1415/180]*0.583[as FWDH]*cos[33.178/2])

D=14.06 nm

FWDH need to be transfer though 1 degree=3.1415/180

For Jade, take the “size only” since it was annealed

XRD: surface evenness will affect the result significantly.

The equation is only fit when the size is about 1-100 especially near 30nm.

Bibliography

[1] Mikael HooK, Xu Tang, Depletion of fossil fuels and anthropogenic climate change-A review, Energy Policy Volume 52, January 2013, Pages 797–809

[2] Goddard Institute of Space Studies NASA. 2009 [cited 2009 November 12]; Available from: http://data.giss.nasa.gov/gistemp/graphs/Fig.A2.txt.

[3] IPCC, IPCC Special Report on Carbon Dioxide Capture and Storage, B. Metz, et al., Editors. 2005.

[4] Sousa Ld. Energy Vision 2050—Part I; 2008 [cited 06.06.13]. Available from: ⟨http://europe.theoildrum.com/node/4485⟩.

[5] Parida B, Iniyan S, Goic R. A review of solar photovoltaic technologies. Renewable and Sustainable Energy Reviews 2011;15:1625–36

[6] http://gcep.stanford.edu/research/exergy/resourcechart.html

[7] Rojas D, Beermann J, Klein S, Reindl D. Thermal performance testing offlatplate collectors. Solar Energy 2008;82:746–57.

[8] Villar NM, López J, Muñoz FD, García ER, Andrés AC. Numerical 3-D heatflux

simulations onflat plate solar collectors. Solar Energy 2009;83:1086–92.

[9] Tang R, Yang Y, Gao W. Comparative studies on thermal performance of water-in-glass evacuated tube solar water heaters with different collectortilt-angles. Solar Energy 2011;85:1381–9.

[10] Bavykin DV, Friedrich JM, Walsh FC. Protonated titanates and TiO2nanostructured materials: synthesis, properties, and applications. Advanced Materials 2006;18:2807–24

[11] Ochiai T, Fujishima A. Photoelectrochemical properties of TiO2 photocatalyst and its applications for environmental purification. Journal of Photochemistry and Photobiology C: Photochemistry Reviews 2012;13:247–62.

[12] Phelan PE, Otanicar TP, Singh H, Taylor RA. Solar energy harvesting using nanofluids-based concentrating solar collector. Journal of Nanotechnology in Engineering and Medicine 2012;3 031003–9.

[13] YousefiT, Shojaeizadeh E, Veysi F, Zinadini S. An experimental investigation on the effect of pH variation of MWCNT–H2O nanofluid on the efficiency of a flat-plate solar collector. Solar Energy 2012;86:771–9.

[14] Liu Z-H, Hu R-L, Lu L, Zhao F, Xiao H-s. Thermal performance of an open thermosyphon using nanofluid for evacuated tubular high temperature air solar collector. Energy Conversion and Management 2013;73:135–43.

[15] Wiki-fuel cell PEM Fuel Cell Technology

[16] Saidur R, Leong K, Mohammad H. A review on applications and challenges of nanofluids. Renewable and Sustainable Energy Reviews 2011;15:1646–68.

[17] Imran Jafri R, Sujatha N, Rajalakshmi N, Ramaprabhu S. Au–MnO2/MWNT and Au–ZnO/MWNT as oxygen reduction reaction electrocatalyst for polymer electrolyte membrane fuel cell, International Journal of Hydrogen Energy. 34 (15) (2009) 6371-76.

[18] Liu H, Song C, Zhang L, Zhang J, Wang H, Wilkinson DP. A review of anode catalysis in the direct methanol fuel cell. Journal of Power Sources 2006; 155:95–110

[19] Diogo M. F. Santos. Quim. Nova, Vol. 36, No. 8, 1176-1193, 2013

[20] De Levie, R.; J. Electroanal. Chem. 1999, 476, 92.

[21] Kreuter, W.; Hofmann, H.; Int. J. Hydrogen Energy 1998, 23, 661.

[22] Rieger, P. H.; Electrochemistry, 1st ed., Prentice-Hall: New Jersey, 1987.

[23] Diogo M. F. Santos. Quim. Nova,Vol. 36, No. 8, 1176-1193, 2013

[24] The production of hydrogen and oxygen through the electrolysis of water; in Scientific American Supplement, Vol. XXXII, no. 819: New York, 1891.

[25] Zeng, K.; Zhang, D.; Prog. Energy Combust. Sci. 2010, 36, 307.

[26] Kreuter, W.; Hofmann, H.; Int. J. Hydrogen Energy 1998, 23, 661.

[27] Emmanuel Zoulias, A REVIEW ON WATER ELECTROLYSIS

[28] Kreuter W, and Hofmann H, 1998, “Electrolysis: the important energy transformer in a world of sustainable energy”, Int. J. Hydrogen Energy 23(8): 661-666.

[29] Neagu C, Jansen H, Gardeniers H, and Elwenspoek M, 2000, ìThe electrolysis of water: An actuation principle for MEMS with a big opportunityî, Mechatronics: 571-581.

[30] Kim, S.; Koratkar, N.; Karabacak, T.; Lu, T. M.; Appl. Phys. Lett. 2006, 88, 263106.

[31] http://en.wikipedia.org/wiki/Electrolysis_of_water

[32] J. O. Bockris, Int. J. Hydrogen Energy 2008, 33, 2129.

[33] Lee, Y., Suntivich, J., May, K. J., Perry, E. E. & Shao-Horn, Y. Synthesis and activities of rutile IrO2and RuO2nanoparticles for oxygen evolution in acid and alkaline solutions.J. Phys. Chem. Lett. 3,399–404 (2012).

[34] J. O. Bockris, T. Otagawa, J. Electrochem. Soc.1984, 131, 290

[35] Isabela C. Man, ChemCatChem2011, 3, 1159 – 1165

[36] J. K. Nørskov, T. Bligaard, J. Rossmeisl, C. H. Christensen, Nat. Chem. 2009, 1, 37;

[37] J. Rossmeisl, Z. W. Qu, H. Zhu, G. J. Kroes, J. K. Norskov, J. Electroanal. Chem.2007, 607, 83.

[38] J. K. Nørskov, J. Rossmeisl, A. Logadottir, L. Lindqvist, J. R. Kitchin, T. Bligaard, H. Jonsson,J. Phys. Chem. B2004, 108, 17 886.

[39] F.S. Galasso, Perovskites and HighTcSuperconductors, Gordon & Brach, New York, 1990.

[40] H.A. Borges, M.A. Continentino, Solid State Commun. 80 (1991) 197.

[41] T.D. McColm, J.T.S. Irvine, Ionics 7 (2001) 116.

[42] V.V. Kharton, F.M.B. Marques, A. Atkinson, Solid State Ionics 174 (2004) 135.

[43] K. Larbaoui, A. Tadjer, B. Abbar, H. Aourag, B. Khelifa, C. Mathieu, J. Alloys Compd. 403 (2005) 1.

[44] F. Tietz, H.P. Buchkremer, D. Stover, J. Electroceram. 17 (2006) 701.

[45] R.V. Vovk, M.A. Obolenskii, A.A. Zavgorodniy, A.V. Bondarenko, I.L. Goulatis,A.V. Samoilov, A. Chroneos, J. Alloys Compd. 453 (2008) 69.

[46] R. Sayers, J. Liu, B. Rustumji, S.J. Skinner, Fuel Cells 8 (2008) 338.

[47] M. Yashima, M. Enoki, T. Wakita, R. Ali, Y. Matsushita, F. Izumi, T. Ishihara, J.Am. Chem. Soc. 130 (2008) 2762.

[48] Y.M. Chiang, D. Birnie, W.D. Kingery, Physical Ceramics: Principles for Ceramic Science and Engineering, John Wiley & Sons, 1997.

[49] A. Chroneos, R.V. Vovk, Oxygen transport in perovskite and related oxides: A brief review

[50] J. O. Bockris, T. Otagawa, J. Electrochem. Soc.1984, 131, 290;

[51] U. Müller, (1993). Inorganic Structural Chemistry, Wiley & Sons Ltd.

[52] C. Frontera, J.L. Garcia-Munoz, A. Llobet, and M.A.G. Aranda, Phys. Rev. B 65, 180405 (2002).

[53] P. Lemmens and P. Millet, Spin – Orbit – Topology, a triptych, in "Quantum Magnetism", Springer, Heidelberg, (2004).

[54] Isabela C. Man, Hai-Yan Su, ChemCatChem2011, 3, 1159 – 1165

[55] Jin Suntivich, HubertA.Gasteiger, Design principles for oxygen-reduction activity on perovskite oxide catalysts for fuel cells and metal–air batteries.

[56] R. N. SINGH, Journal of Applied Electrochmeistry, 24 (1994) 149-156

Curriculum Vita

Ning Wang was born on Aug, 1990 in Suzhou, Jiangsu Province, China. He received her Bachelor's Degree at Beijing University of Chemical Technology, Beijing majoring in Applied Chemistry in 2012. He joined the chemical and biomolecular engineering at Johns Hopkins University in 2012, started to work in Professor Chao Wang's group. His research involved catalysts applied in oxygen evolution reaction.

Email: nwang16@jhu.edu